Journal of Hydrology 621 (2023) 129672

Contents lists available at ScienceDirect

Journal of Hydrology

journal homepage: www.elsevier.com/locate/jhydrol

Research papers

Experimental and molecular investigation of water adsorption controls in marine and lacustrine shale reservoirs

Chima Finnian Ukaomah [a,b,c], Mengdi Sun [a,b,*], Zhejun Pan [a], Mehdi Ostadhassan [a,d,e], Bo Liu [a], Qingbang Meng [b,*], Mohammed Dahiru Aminu [f], Michael Fischer [g,h,i]

[a] Key Laboratory of Continental Shale Hydrocarbon Accumulation and Efficient Development, Ministry of Education, Northeast Petroleum University, Daqing 163318, China
[b] Key Laboratory of Tectonics and Petroleum Resources, Ministry of Education, China University of Geosciences, Wuhan 430074, China
[c] Department of Energy and Mineral Engineering, The Pennsylvania State University, University Park, PA, United States
[d] Institute of Geosciences, Marine and Land Geomechanics and Geotectonics, Christian Albrechts Universität, Kiel 24118, Germany
[e] Department of Geology, Ferdowsi University of Mashhad, Mashhad, Iran
[f] Clean Air Task Force, Boston, MA 02109, United States
[g] Crystallography and Geomaterials Research, Faculty of Geosciences, University of Bremen, Germany
[h] Bremen Center for Computational Materials Science, University of Bremen, 28359 Bremen, Germany
[i] MAPEX Center for Materials and Processes, University of Bremen, 28359 Bremen, Germany

ARTICLE INFO

Keywords:
Water vapor adsorption
Shale reservoirs
Organic matter
Pore size distribution
Water distribution
CO_2 storage

ABSTRACT

The restriction of hydrocarbon migration within shale reservoirs by pre-adsorbed water necessitates an investigation into water adsorption control mechanisms within shales. In this study, water vapor adsorption isotherms obtained from marine and lacustrine shale samples along with isotherms from their organic matter and experimentally verified kerogen molecular models were used to evaluate water adsorption mechanisms, with simulated wet kerogen-quartz nanocomposites. Furthermore, these were also used to investigate organic matter-inorganic interaction controls on water adsorption. Pore size distribution (PSD) controls on water distribution in organic matter were obtained via water vapor adsorption and low-pressure nitrogen adsorption analysis, along with small angle neutron scattering (SANS) analysis. The results reveal water adsorption is linked to changes in mesopore volume within organic matter and porosity in kerogen models. PSD obtained from the shales only reveal mesopore controls at high RH, with water adsorption mainly controlled by oxygen functional groups in organic matter pores and swelling clays. Inorganic controls on water adsorption are also observed in adsorbed water not tightly bound to the shale surface due to a high montmorillonite content in clay interlayers, and organic matter interaction with quartz with a negative relationship between the adsorbed water and the quartz content. Collectively, these findings indicate that CO_2 migration in shale reservoirs could be inhibited by water that is distributed in potential CO_2 adsorption sites within organic matter pores and montmorillonite.

1. Introduction

Understanding the impact of pore-scale water distribution relative to other immiscible fluids present within shale formations (Tokunaga, 2009), is critical to hydrocarbon exploitation of shale reservoirs. This is especially important when changes in adsorption selectivity of hydrocarbon mixtures due to the presence of pre-adsorbed water (Di Lella et al., 2006), is factored into the hydrocarbon exploitation process for shale reservoirs. This is because, unlike conventional reservoirs, shales are characterised by fluid interactions controlled by capillary forces, along with inorganic and organic content (Dehghanpour et al., 2013).

While organic content influence on water adsorption is found in an induction of wettability complexity within shales (Liang et al., 2016), that of inorganic content is seen in effective permeability alteration due to clay mineral hydration (Dehghanpour et al., 2012; Zolfaghari et al., 2017a). However, it is important to note that adsorption forces also play a role in water uptake for water wet organic rich shales which are swelling clay deficient (Dehghanpour et al., 2012), with studies noting the physical and chemical nature of water interactions with organic matter (Zhou et al., 2016). These findings along with the critical role

* Corresponding authors.
E-mail addresses: sunmd@nepu.edu.cn (M. Sun), mengqb@cug.edu.cn (Q. Meng).

https://doi.org/10.1016/j.jhydrol.2023.129672
Received 4 December 2022; Received in revised form 28 April 2023; Accepted 3 May 2023
Available online 13 May 2023

organic and inorganic components play in low hydraulic fracture water recovery (Hu et al., 2015), necessitate an analysis of mechanisms behind water adsorption.

These mechanisms can be experimentally analysed via sorption–desorption isotherms described by a relationship between relative vapour pressure and water content at a given temperature (Arthur et al., 2016; De La Llave et al., 2010; Shen et al., 2018; Wan et al., 2016). These isotherms, which are usually linked to a hysteresis loop having a shape influenced by temperature, pore size, and pore wall hydrophyphilicity (De La Llave et al., 2012, 2010; Striolo et al., 2005), have been used to determine inorganic and organic pore size distribution (PSD) (Chen et al., 2020; Zolfaghari, Dehghanpour, & Xu, 2017; Zolfaghari & Dehghanpour, 2015), and to experimentally verify water condensation differences in inorganic and organic pores as being responsible for a higher possession of gas storage accessible pores by the latter (Li et al., 2017).

However, while experimental isotherms obtained from different shale formations have revealed a stronger relationship between inorganic content and water vapor adsorption capacity (Wang et al., 2019), and a relationship between organic content and hysteresis loop variability (Yang et al., 2020a), the mechanisms behind variations in inorganic or organic pore influence on water vapor sorption isotherms for different shale reservoirs are yet to be analysed. This is even more critical under higher temperature conditions which is difficult to impose in an experiment. This is despite experimental suggestions of water vapor diffusion coefficient in shales that is usually enhanced at high temperatures (Sang et al., 2020a). Thus, the superiority of simulated isotherms over those obtained from experiments being found in an imposition of higher temperature conditions has led to the usage of a combination of experimental and simulated water adsorption isotherms to analyse mechanisms behind water adsorption (Striolo et al., 2005).

Apart from high temperature limitations, another demerit of experimental water adsorption is inaccuracy when used to determine capillary pressure since water sorption in shales is controlled by surface chemistry not pore size (Lahn et al., 2020; Seemann et al., 2017). This is despite suggestions of shale PSD obtained from water sorption–desorption isotherms being superior to those obtained from experimental techniques like mercury injection capillary pressure analysis (MICP) (Zolfaghari and Dehghanpour, 2015), and vapor sorption experiments. These methods have been used to note water adsorption in shales as being moderately controlled by micropores (<2 nm) and dominantly influenced by mesopores (2 – 50 nm) (Sang et al., 2020b), with the former having a major influence on monolayer water adsorption (Bai et al., 2020). Thus, an investigation into water adsorption controls in shale reservoirs necessitates a conjunction of experimental water sorption–desorption isotherms with various techniques which can be used to characterise shale nanopore structure.

These techniques include the usage of a combination of water vapor sorption–desorption isotherms with low-pressure nitrogen adsorption and small-angle neutron scattering (SANS) to observe micro and mesopore controls on water adsorption in shales (Sang et al., 2018a). Furthermore, a recent usage of SANS to reveal organic and inorganic controls on water condensation in shales (Sang et al., 2020b), suggests an insight into water sorption controls in organic rich shales can be obtained by combining an experimental characterization of organic and inorganic pore structure with water sorption–desorption.

Studies have also emphasized the need for investigations into temperature influence on water sorption in shales via thermodynamic analysis and modelling of the two phases of water adsorption (Tang et al., 2017). The efficacy of such an approach can be found in the usage of modelled experimental water vapor isotherm data along with an evaluation of isosteric heat determined via the Clausius-Clapeyron equation (Duan and Li, 2018; Sang et al., 2019a).

In this study, low-pressure nitrogen adsorption and small-angle neutron scattering analysis along with experimental water vapor isotherms are carried out on the organic matter (OM) and shale samples of the marine Longmaxi shale, lacustrine Qingshankou and Chang 7 shale oil formations. These methods are performed in conjunction with high temperature simulations of water adsorption in experimentally verified kerogen models of each formation to analyse water adsorption mechanisms for shale reservoirs. Water adsorption is discussed using the modelled isotherms along with isosteric heat, pore structure and composition controls obtained from SANS and low-pressure nitrogen adsorption experimental observation of shale nanopores. Furthermore, nanocomposites created with kerogen models and quartz are also used to evaluate water distribution controls in the shale formations. Ultimately, we believe observations that is obtained in this study can be significant for CO_2 storage capacity evaluations in shale reservoirs.

2. Methodology

2.1. Samples and experimental techniques

Organic matter in Longmaxi shales was formed in a deep water continental shelf characterised by an oxygen deficient environment which aided a high biogenic yield derived from blooming algae, radiolarians, sponges, pens, and other organisms (Dong et al., 2018). In comparison to this marine derivation of organic matter, the lacustrine Chang 7 shales comprises of organic matter generated within a lacustrine-delta from phytoplankton and terrigenous plants (Chen et al., 2019). Similarly, organic matter accumulation in the lacustrine Qingshankou shales has also been stated as being due to an occurrence of good preservation conditions along with a high primary productivity and terrigenous input (Xu et al., 2019).

Shale samples analysed in this study were obtained from the Longmaxi, Qingshankou, and Chang 7 formations. Offcuts of each sample were crushed into powdered form (<200 mesh) and used for total organic carbon (TOC), vitrinite reflectance, and X-ray diffraction measurements via procedures prescribed by Sun et al. (2016). The mineralogical and organic matter information obtained is shown in Table 1. Furthermore, in order to ascertain organic carbon content influence on water adsorption, solid organic matter (OM) which includes kerogen and bitumen, was also extracted from offcuts of each shale sample via chemical extraction procedure following Zhang et al (Zhang et al., 2020a; Zhang et al., 2020b).

2.1.1. Low pressure nitrogen adsorption and SANS experiments

Low pressure N_2 adsorption analysis was undertaken on weighed powdered organic matter and shale samples (35 – 80 mesh) using the Quantachrome Autosorb-1 apparatus. The procedure undertaken as described in our previous study (Finnian Ukaomah et al., 2022). While several studies have made optimal mesh recommendations based on low pressure adsorption data in shale samples with various mesh sizes (Hazra et al., 2018; Mastalerz et al., 2017), the size of mesh that was used in this study is < 200 which is generally recommended for low pressure N_2 adsorption analysis of shale reservoirs (Han et al., 2016).

Other sample preparation procedures include moisture removal via degassing of the powdered samples at 110 °C for 5 h in a vacuum. Considering the influence of temperature on low pressure adsorption data (Holmes et al., 2017), degassing temperature was 110 °C which is proposed for shale samples (Singh et al., 2021). Degassing was followed by measurement of nitrogen adsorption/desorption at 77.3 K within relative pressures calibrated with saturated vapor pressure of the gas. The density functional theory (DFT) and the Brauner-Emmet-Teller (BET) model were then respectively used to obtain the mesopore-macropore volume (1.4 – 300 nm) and surface area from the nitrogen adsorption data (Lowell et al., 2004; Thommes et al., 2015).

The SANS experiments were done with the SANS apparatus at the China Spallation Neutron Source (CSNS) with fixed sample to detector distance at 4 m, covering a 0.005 $Å^{-1}$ to 0.6 $Å^{-1}$ Q range via neutrons that are received at different incident wavelengths (1 – 10 Å). Powdered shale samples (35 – 80 mesh) containing organic matter and extracted organic matter were respectively oven dried for 48 h at 60 °C before

Table 1
Basic compositions of shale samples.

Formation	Sample ID	Depth (m)	TOC (*wt.%*)	R_0 (%)	Whole rock minerals (*wt.%*)						Clay mineral content (*wt.%*)					
					Clays	Quartz	Plagioclase	Calcite	Dolomite	Pyrite	Other	K	C	I	I/S	% S_m
Longmaxi	JY11-4	2338.1	2.5	2.77	27.8	52.8	5.6	3.6	5.4	4.8	0	0	0	33	67	15
Chang 7	Z22-48	1606.7	4.2	1.21	66.1	25.2	4.1	0	0	1.4	3.2	6	0	12	82	20
Qingshankou	3HC-4	2459.53	3.8	1.40	60.8	13.1	21.2	0.3	0.5	2.5	1.6	0	6	6	88	5

*TOC = Total organic carbon, K = kaolinite, C = Chlorite, I = Illite, I/S = mixed layer illite and smectite, $\%S_m$ = percentage of montmorillonite in mixed clays.

being loaded into the SANS apparatus to obtain their pore structure information.

The scattering length density (SLD) for each shale sample was obtained by volume averaging the SLD value of all shale components (Sun et al., 2017). The SANS datasets were analysed with the Igor Pro software via a polydisperse size distribution model (PDSM) that assumes shale pores are randomly distributed spheres (Sun et al., 2022). The relationship between the Q value from the SANS data and the shale pore radius (R) was established via R = 2.5/Q (Radliński et al., 2000).

2.1.2. Water vapor adsorption isotherm measurement

Sample preparation for water vapor sorption analysis (WVA) involved weighed 35 – 80 mesh of the samples (both shale and organic matter) getting oven-dried at 100 °C for 48 h. This removal of initial moisture content before conducting the WVA was done to prevent irreversible pore structure changes. The WVA isotherms were then obtained from gravimetric measurements of water vapor uptake and loss as a function of relative humidity (RH) in a Quantachrome Aquadyne DVS sorption analyser at three temperatures (25 °C, 35 °C, and 45 °C), with RH set from 2% to 95%.

Importantly, the 2% RH was achieved before starting the experiment via usage of a 100 – 150 cm^3/min flow rate. Furthermore, while change in sample mass during adsorption and desorption processes was sequentially recorded with a 0.1 μg ± 1% accuracy, sample adsorption/desorption equilibrium conditions at any value of RH comprised<0.001 %/min sample mass change.

2.2. Adsorption models

2.2.1. GAB model

To mathematically describe water adsorption in the samples, the Guggenheim (Guggenheim, 1963), Anderson (Anderson, 1946), and de Boer (De Boer, 1953), modified extension of the BET model (Brunauer et al., 1938), is applied over the entire range of RH. This GAB model differs from the BET theory (Brunauer et al., 1938) by assuming that the heat from adsorption of multilayers is less than the heat due to liquefaction, and sorbate molecules beyond the monolayer will continue to interact with the sorbent surface (Sang et al., 2019b). The model introduces a parameter K into the adsorbed amount V (mg/g) via (Sang et al., 2019b):

$$V = \frac{V_m K C_{GAB} R_h}{(1 - KR_h)[1 - KR_h + C_{GAB} KR_h]} \tag{1}$$

Where V_m represents the GAB monolayer capacity (mg/g); C_{GAB} a constant linked to the heat of adsorption; K a constant linked to adsorption energies within multilayer adsorption sites; R_h the relative humidity of water vapor.

2.2.2. Freundlich model

This model assumes that all adsorption sites of a porous solid act simultaneously despite being unevenly distributed (Freundlich, 1931). The model is linearly defined as (Sang et al., 2019b):

$$lnV = lnk + \frac{1}{n} lnR_h \tag{2}$$

Where V represents adsorbed mass (mg/g); k and n are constants obtained from the intercept (lnk) and slope ($\frac{1}{n}$) of linearly relating lnV vs lnR_h.

2.2.3. Hysteresis characterisation

A hysteresis loop is an observed difference in adsorption and desorption isotherms (Tang et al., 2017; Yang et al., 2020c). In this study, hysteresis in water vapor isotherms obtained from shale and OM samples is quantitively described via the Area Hysteresis Index (AHI) as follows (Tang et al., 2017):

$$AHI = \frac{A_{de} - A_{ad}}{A_{de}} \times 100 \tag{3}$$

Where A_{de} and A_{ad} respectively represent the area under the adsorption and desorption isotherms.

2.2.4. Derivation of pore size distribution from water vapor adsorption

Several studies have used the Kelvin equation to characterize PSD from WVA adsorption isotherms (Chen et al., 2021; Hou et al., 2021; Yang, Jia, He, et al., 2020a; Zolfaghari, Dehghanpour, & Xu, 2017). Chen et al. (2021) suggested the insensitivity of the PSD obtained via WVA from natural and organic free shale samples via the Kelvin equation to the changes in the contact angle. In addition, despite the speculation of uniform wettability within the pores, without any condensation within the organic pores, WVA PSD obtained via the Kelvin equation can be used in conjunction with the PSD from low pressure N_2 adsorption to acquire the organic PSD (Zolfaghari et al., 2017b). Thus, in this study, we used the Kelvin equation to characterise WVA PSD from shale and organic matter samples.

The equation exploits a relationship between RH and pore size when capillary condensation takes place within the pore (Zolfaghari et al., 2017b):

$$\ln\left(\frac{1}{RH}\right) = \frac{2\gamma V_m \cos\theta / TR}{r_p} \tag{4}$$

Where RH represents relative humidity; γ surface tension; V_m liquid molar volume; T temperature; θ the contact angle; R and r_p universal gas constant and pore radius. Since pore size is not dependent on the numerator (Yang et al., 2020a), the pore size of condensed water vapor filled capillary pores is obtained via (Zolfaghari et al., 2017b):

$$r_p = -\frac{RT[\ln(\frac{1}{RH})]^2}{2\gamma V_m \cos\theta} \times \frac{d\varnothing_w}{dln(\frac{1}{RH})} \tag{5}$$

Where $\varnothing_w$ represents pore volume fraction of pore sizes less than or equal to r_p, which does not represent the true pore diameter. Since water vapor adsorption on pore surfaces also takes place via multilayer adsorption before capillary condensation, the thickness formed from the former is considered into pore diameter calculations via:

$$d = 2(r_p + t) \tag{6}$$

With Halsey's equation used to obtain the adsorption layer thickness t as follows:

$$t = 0.354[-5\ln(\frac{p}{p_0})]^2 \quad (7)$$

2.3. Molecular simulation

Molecular simulation is a theoretical method of analysing organic matter interaction with fluids under higher temperature conditions difficult to impose in an experiment. Thus, in order to ascertain organic matter influence on water adsorption mechanisms in the shale formations, water adsorption on their experimentally verified molecular kerogen models is simulated at 525 K on the Materials Studio (MS) application. Furthermore, simulation of water distribution in nanocomposites respectively comprising the kerogen models and quartz was also utilized via MS to evaluate water distribution controls.

2.3.1. Molecular models

Experimentally verified kerogen models used include the Silurian model ($C_{194}H_{96}O_9N_4S_7$) by Huang et al., (2017), the type II Chang 7 oil shale kerogen model ($C_{300}H_{297}O_{18}N_{13}S_{10}$) recently proposed by Wu & Xu (2022), and the oil prone Qingshankou kerogen model ($C_{156}H_{159}N_3O_{10}$) proposed by Cao et al., (2021). To create 3-D structures of these models, ten molecules of each model were respectively initially geometrically optimized using the Condensed-phase Optimized Molecular Potentials for Atomistic Simulation Studies (COMPASS) forcefield before being placed in an amorphous cell with an 0.1 g/cm^3 initial density and 300 K temperature The forcefield uses a 6–9 Lennard-Jones potential parameterization with mixing rules described in previous studies (Sun, 1998).

The amorphous cell setup exceeds the 1700 atoms/cell requirement prescribed by previous studies (Ungerer et al., 2015). In order to obtain configurations with the global lowest energy, the cells were respectively further optimized and relaxed with the COMPASS forcefield via annealing and molecular dynamics procedures prescribed by Huang et al., (2018). However, it is critical to note that typical reservoir condition of each formation obtained from stated temperature and pressure gradients, were used for final NPT molecular dynamics simulations of the kerogen molecules (Fig. 1), with final relaxation of the Longmaxi molecules at 360 K and 23.6 MPa (Huang et al., 2017), the Chang 7 model at 346.84 K and 16.9 MPa (Li et al., 2013; Zhao et al., 2021), and Qingshankou kerogen molecules at 373 K and 42.5 MPa (Feng et al., 2019; Zhang et al., 2020a; Zhang et al., 2020b). For all simulations, the Nose-Hoover thermostat was used to control the system temperature (Hoover, 1985), with pressure imposed via the Berendsen barostat (Berendsen et al., 1998).

2.3.2. Water adsorption simulation

Water adsorption on the kerogen models was performed via Grand Canonical Monte Carlo (GCMC) simulations conducted on the MS sorption module. The simulations are characterised by chemical potential, volume, and temperature system parameters being fixed. The chemical potential is converted to vapor pressure P (Zhang et al., 2021), which is calibrated with water saturated vapor pressure (P_{sat}) determined from the National Institute of Standards and Technology (National Institute of Standards and Technology, 2018). The system relative humidity was therefore obtained as P/P_{sat}.

Water adsorption simulation was then carried out from 5% RH to 95% RH at 525 K with 1×10^7 Monte Carlo steps (5×10^6 steps for equilibration and 5×10^6 for ensemble average). Furthermore, while the Ewald summation method was used to describe electrostatic interactions with an accuracy of 0.001 kcal mol^{-1}, Van der Waals atom method-based interactions between different molecules were determined within a 15.5 Å cut-off distance.

The adsorbed water content S_w was obtained from the number of water molecules N_w adsorbed on the kerogen models via (Zhang et al., 2021):

$$S_w = \frac{N_w \times M_w}{N_A \times A} \quad (8)$$

Where water molar mass (g/mol) is represented by M_w; N_A represents the Avogadro constant (mol^{-1}); and A the surface area of simulated kerogen (m^2). The COMPASS forcefield which has been used to simulate the interaction of fluids with kerogen and quartz (Sui & Yao, 2016; Wu et al., 2013), was used to parameterize water adsorption in GCMC simulations.

2.3.3. Water distribution in nanocomposites

To determine water distribution controls in the shale reservoirs, organic–inorganic nanocomposite models were prepared by coupling ten molecules of each kerogen model with quartz. Similar to previous simulations of kerogen-mineral interactions (Faisal et al., 2021), the α-quartz unit cell (cell dimensions are a = b = 4.9134 Å, c = 5.4052 Å, and α = β = 90°, γ = 120°) on MS was used to create a 4 × 8 × 1 supercell used to construct the nanocomposite model.

Wet nanocomposites were then built by using the packing task on MS to insert 32 water molecules with the density set to 0.4 g/cm^3 (Fig. 2). NVT molecular dynamics simulation were then performed at 300 K and 400 ps to bring the wet model to equilibrium which was attained when temperature vs. simulation time exhibit fluctuations in proximity to the simulation temperature after rising and approaching an equilibrium

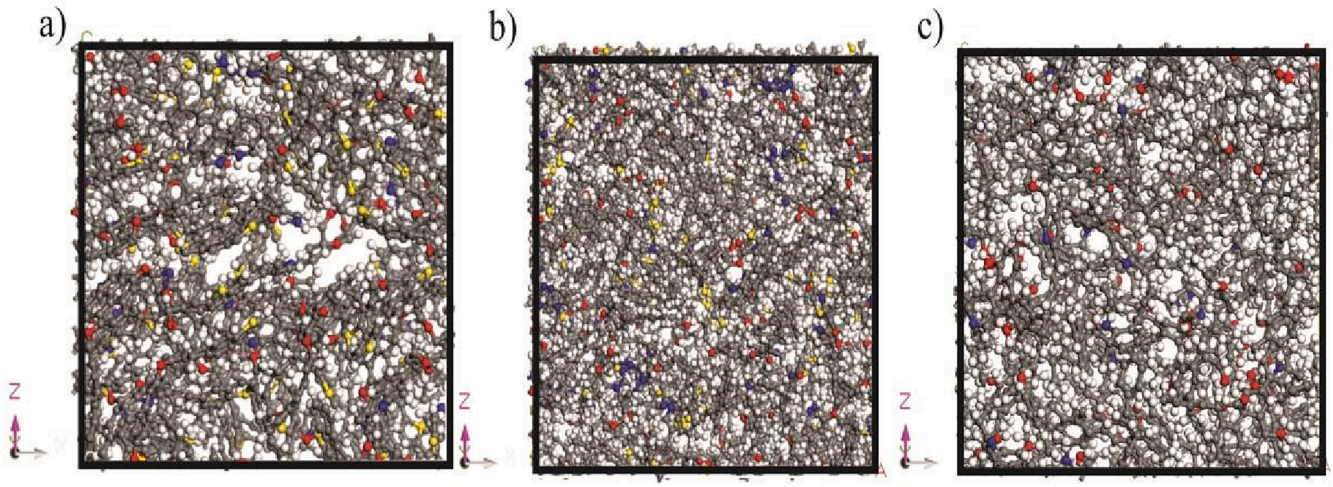

Fig. 1. Experimentally verified a) Longmaxi b) Chang 7 and C) Qingshankou kerogen models after NPT simulations. Atom representation: Carbon is grey, oxygen atoms are red, hydrogen atoms are white, sulphur atoms are yellow.

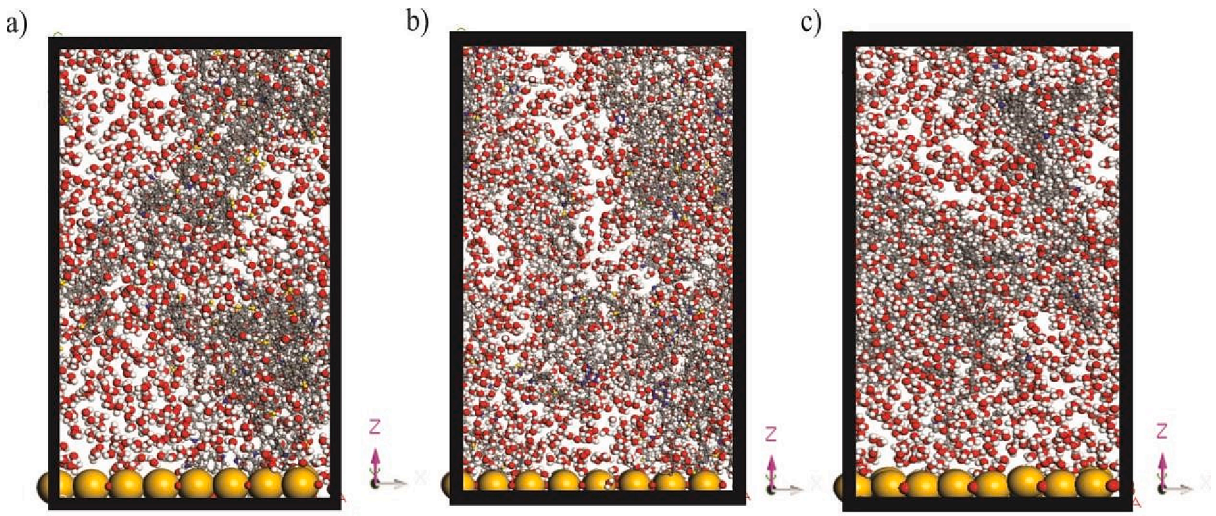

Fig. 2. Proposed kerogen-quartz nanocomposites for a) Longmaxi b) Chang 7 and c) Qingshankou kerogen models. Silica on the quartz is differentiated from sulphur in kerogen by bigger yellow-coloured atoms.

point.

To analyse heat treatment controls on water distribution, the nanocomposites were further subjected to NVT 200 ps MD simulations at 400 K. After MD simulations, the quartz surface becomes unfixed, and frames from the NVT trajectory are used to obtain the concentration profile from the nanocomposite. The MD simulation of water distribution was done via COMPASS forcefield parameterization at a 0.1 fs time step.

2.3.4. *Kerogen model validation*

A comparison of data from the simulated kerogen models with experimental results are done to ensure their validity for this study. In the first phase, a comparison of kerogen density reveals the 1.307 g/cm^3 and 1.18 g/cm^3 density respectively obtained from the Longmaxi and Qingshankou kerogen as falling within experimentally measured density ranges (1.18 g/cm^3 to 1.35 g/cm^3) for mature type II kerogen (Okiongbo et al., 2005), with the density obtained from the Chang 7 kerogen model in this study (that is, 1.12 g/cm^3) being very close to this range.

Further validation was also carried out with a helium probe to estimate kerogen porosity according to procedures prescribed by Guo et al. (2020). This involved using the Conolly surface to obtain the free pore volume which was then used to determine the kerogen matrix porosity (Fig. 3). The porosities, respectively, obtained for the Longmaxi (21.78 %), Chang 7 (17.22 %), and Qingshankou models (14.67 %) all fall within the range experimentally obtained from the Barnet shale (4.45% – 22.50%) (Loucks et al., 2009).

In addition, the H/C, O/C, N/C, and S/C atomic ratios in each model is equivalent to those from experimentally characterized kerogen in each formation. This includes ratios from Longmaxi kerogen model (0.495, 0.046, 0.02, 1.86, 0.036) being equivalent to those obtained from a highly mature type II kerogen (Huang et al., 2017), and Chang 7 model atomic ratios (0.99, 0.06, 0.043, 0.033) close to those of type II oil prone Chang 7 kerogen (Wu & Xu 2022). Atomic ratios from the sulphur deficient Qingshankou model H/C, O/C, and N/C (1.101, 0.064, 0.019) resemble those experimentally proposed for oil prone kerogen from the Qingshankou formation (Cao et al., 2021). Overall, the atomic ratios in the kerogen models indicate a thermal maturity which varies from Longmaxi > Chang 7 > Qingshankou.

3. Results

3.1. *Pore structure (low-pressure nitrogen adsorption, WVA, and SANS)*

A correlation of hysteresis loops obtained from shale N_2 adsorption and desorption isotherms (Fig. 4a) with IUPAC recommendations (Sing

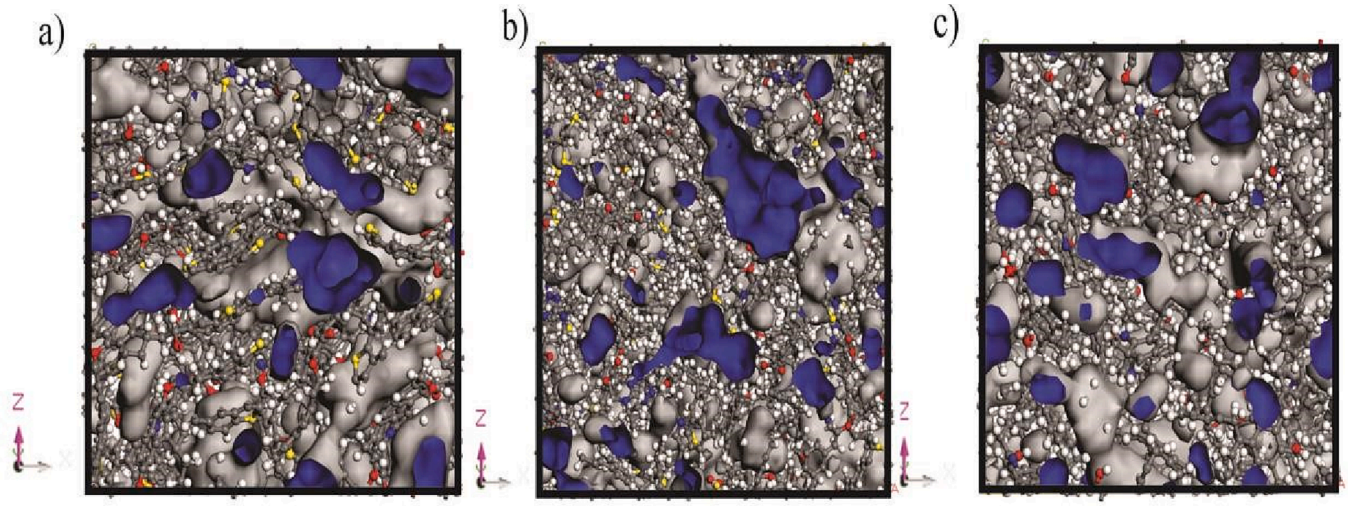

Fig. 3. Free pore volume in a) Longmaxi b) Chang 7 and C) Qingshankou kerogen models. Blue regions represent pore volumes.

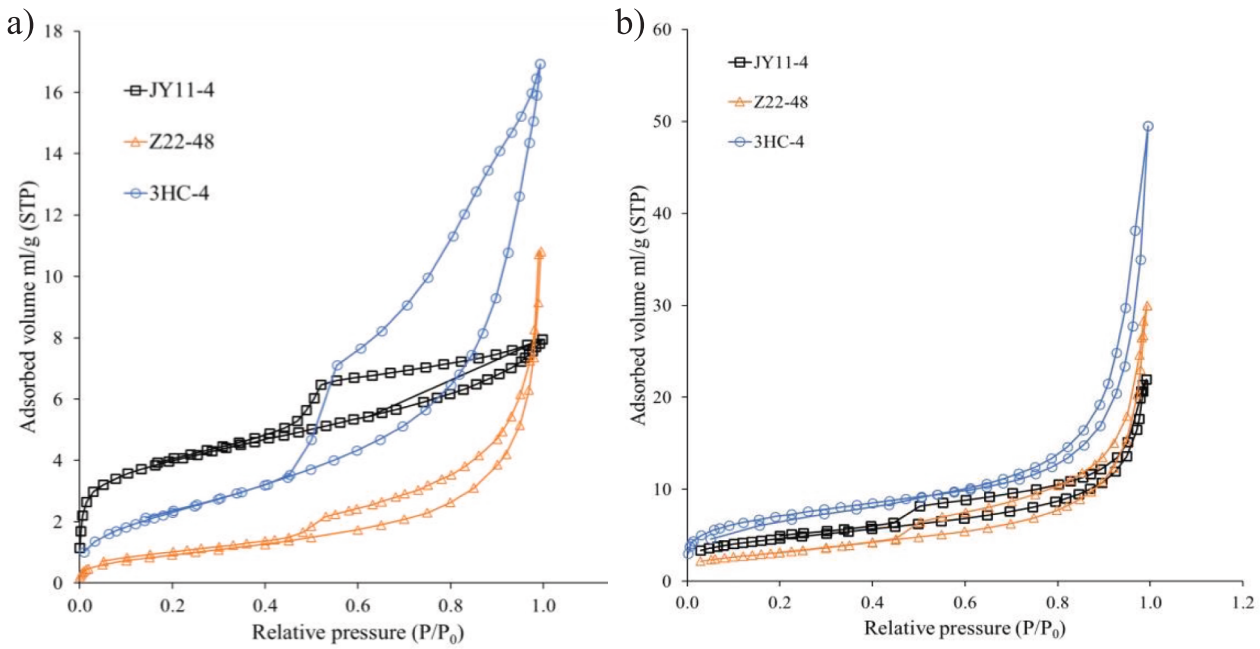

Fig. 4. Nitrogen adsorption isotherms obtained from a) shale and b) organic matter samples.

et al., 1985), reveals the presence of inkbottle and slit shaped pores, with the latter also observed to be dominant in the organic matter samples (Fig. 4b). Table 2 reveals shale mesopore-macropore volume varies from 0.015 ml/g to 0.019 ml/g, with organic matter specimens characterised by volume that varies from 0.02 ml/g to 0.032 ml/g. In addition, while BET surface area in the shales vary from 3.48 m^2/g to 12.86 m^2/g, organic matter exhibited a surface area that varies from 11.32 m^2/g to 24.54 m^2/g. Porosity obtained from N_2 adsorption on the shale samples was found from 2.9 % to 4.6 % (Table 2).

SANS profiles obtained from shale samples reveal scattering curves which obey a power law within a Q range of ~ 0.001 to ~ 0.1 (Fig. 5). Power law deviations observed in the scattering profiles are probably due to long neutron wavelength (12 Å) (Radlinski et al., 1999), micro-pore scattering (Sang et al., 2018a), and scattering from hydrogen atoms in organic matter or residual moisture within the pores (Mastalerz et al., 2012; Radlinski et al., 1999). A comparison of scattering profiles also reveals that a higher flat scattering background at high Q values observed in shale sample Z22-48 is probably due to high micro-scale heterogeneity or water bound within the clay minerals and organic matter. The former is exemplified by the shale sample having the highest percentage of montmorillonite within mixed clays (Table 1).

A comparison of porosities obtained from both SANS and N_2 adsorption (Table 2) reveals a similar variation in porosity obtained from PDSM porosity and N_2 for the shale samples, with higher values from the former being related to the SANS experimental technique that

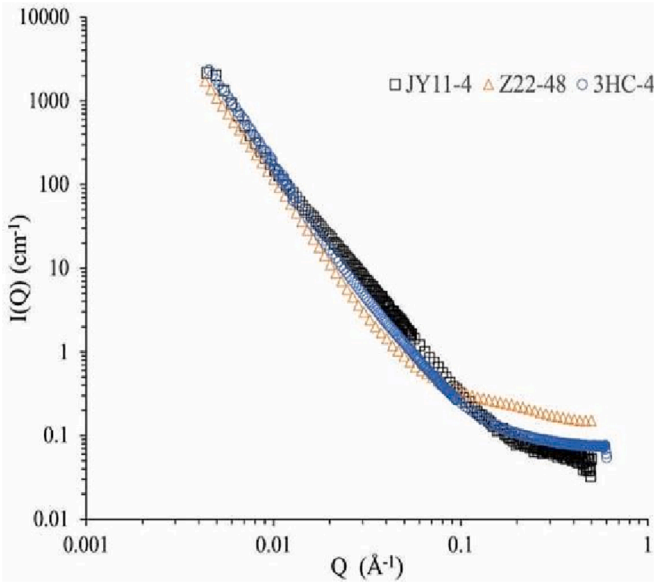

Fig. 5. SANS raw profiles obtained from the shale samples.

Table 2
Pore structure obtained from low pressure nitrogen adsorption and SANS analysis of shale and organic matter.

Sample ID	Shale bulk density (g/cm^3)	Organic matter N_2 adsorption		Shale N_2 adsorption			Shale SANS measurements		
		Pore volume (ml/g) (1.4 – 300 nm)	BET surface area (m^2/g)	Pore volume (ml/g) (1.4 – 300 nm)	**Porosity (%)	BET surface area (m^2/g)	PDSM Porosity (%)	Surface area (m^2/g)	*Fraction of closed pores (%)
JY11-4	2.45[a]	0.02	16.04	0.015	3.7	12.86	4.44	36.5	16.67
Z22-48	2.41[a]	0.032	11.32	0.012	2.9	3.48	4.43	52.3	34.54
3HC-4	2.43[a]	0.05	24.54	0.019	4.6	8.83	5.51	50.1	16.52

*Fraction of closed pores = (PDSM porosity – N_2 porosity)/PDSM porosity.
** Calculated from bulk density.
[a]Obtained from mercury injection capillary pressure measurements of shale cores.
[b]Calculated from PDSM porosity using organic matter density prescribed by Sun et al [1].

basically measures both accessible and inaccessible pores within the samples. This measurement difference also explains as why surface area measured with SANS varies widely compared to what was found via N_2.

Pore volume distribution obtained from WVA, SANS, and N_2 adsorption are showing a similar trend over a 1 nm to 100 nm pore size range (Fig. 6), for all shale samples except JY11-4 which is characterised by N_2 pore volume distribution that steadily decreases within this pore size range. Another exception is also observed in SANS and WVA revealing sample Z22-48 as being characterised by an initial increase in pore volume at a lower pore size range compared to the remaining samples. Considering the organic matter samples (Fig. 7), apart from showing a comparable pattern, pore volume distribution obtained from WVA are higher than those obtained from N_2 adsorption for all samples except sample 3HC-4. This variation in pore volume is negatively linked to the 3HC-4 > Z22-48 > JY11-4 variation in mesopore-macropore volume observed within the organic matter samples (Table 2). That is, larger differences in pore volume are observed in organic matter samples having low mesopore-macropore volumes.

3.2. Water vapor isotherm hysteresis characterisation

Water vapor adsorption/desorption isotherms obtained from all shale and organic matter samples over the entire RH range (5% to 95%) at three temperatures (25 °C, 35 °C, and 45 °C) reveal type II adsorption isotherms with type H3 hysteresis loops (Fig. 8 and Fig. 9) based on IUPAC classifications (Sing et al., 1985). These isotherms are divided into a low RH region dominated by monolayer adsorption (RH < 0.2), intermediate region after termination of monolayer adsorption (RH < 0.8), and a high RH region dominated by capillary condensation (RH varies from 0.8 to 0.95) (Hou et al., 2021).

All samples were also observed to be characterised by pronounced hysteresis behaviour at high RH conditions due to multilayer adsorption, with water adsorption/desorption isotherms obtained from some samples not converging towards minimum values and remaining open under low RH conditions. This lack of convergence is profound in isotherms respectively obtained from shale samples JY11-4 and Z22-48 at 25 °C and 35 °C (Fig. 8a and 8b), and isotherms obtained from organic matter sample JY11-4 at all experimental temperatures (Fig. 9).

A comparison of AHI values from shales at all experimental temperatures (Table 3) reveals JY11-4 has the highest AHI value due to being characterised by maximum hysteresis which occur at a higher RH. In the organic matter samples (Table 4), this phenomenon is only observed at 45 °C with sample Z22-48 having the highest AHI values at 25 °C and 35 °C. In addition, a plot of AHI vs. temperature for both shale and organic matter samples (Fig. 10a and 10b) reveals sample JY11-4 having a weaker negative relationship of these two parameters compared to other samples.

3.3. Modelled adsorption isotherms from experiment

WVA isotherms are fitted with the GAB and Freundlich models to evaluate organic and inorganic controls on water sorption in the shale formations. While parameters obtained from GAB and Freundlich fitted WVA isotherms of the shale (Figs. 11 and 12) are presented in Table 3, those from organic matter samples (Figs. 13 and 14) are illuminated in Table 4. Freundlich n parameters being<1 for all samples indicates an overall low affinity for water, and a similar observation obtained for the correction factor K which confirms that multilayer adsorption is weaker compared to adsorption within the monolayer (Sang et al., 2019b).

3.3.1. Shales

For the shale samples, GAB fitting results at all temperatures reveal a monolayer moisture content (V_m) varying in the order of 3HC-4 > Z22-48 > JY11-4 (Table 3). In addition, sample JY11-4 is observed as having the highest binding strength parameter (C_{GAB}) at all experimental temperatures.

Freundlich fitting of the shale isotherms at all temperatures reveals the existence of two adsorption regimes with k values obtained from the entire RH range between those of low (>70% RH) and high (<70% RH) adsorption strength. k values obtained at < 70% RH are observed to follow 3HC-4 > Z22-48 > JY11-4, with a similar trend only observed under > 70% RH conditions at 45 °C as the k values obtained at other temperatures show 3HC-4 > JY11-4 > Z22-48 (Table 3).

3.3.2. Organic matter

For the extracted organic matter samples (Table 4), GAB fitting reveals a V_m exhibiting JY11-4 > Z22-48 > 3HC-4 at 35 °C and 45 °C, with the parameters showing JY11-4 > 3HC-4 > Z22-48 at 25 °C. In addition, apart from values at 45 °C which reveals JY11-4 as having a value higher than other samples, C_{GAB} values obtained from the organic samples are observed as: Z22-48 > JY11-4 > 3HC-4.

Similar to the shale samples, Freundlich fitting of the organic matter isotherms (Table 4) also was found that k values obtained from the entire RH range within those obtained from < 70% RH and > 70% RH, with k values obtained at both RH ranges observed to follow JY11-4 > Z22-48 > 3HC-4 at all experimental temperatures.

3.4. Isosteric heat of adsorption

Several studies have used isosteric heat of adsorption to gain an insight into how adsorbed water interacts with the shale surface (Duan and Li, 2018; Sang et al., 2019b). Thus, in this study we used the slope of ln*(p)* vs. *1/T* plots to obtain the isosteric heat of adsorption for shale and kerogen samples via the Clausius-Clapeyron equation (Sang et al., 2019b):

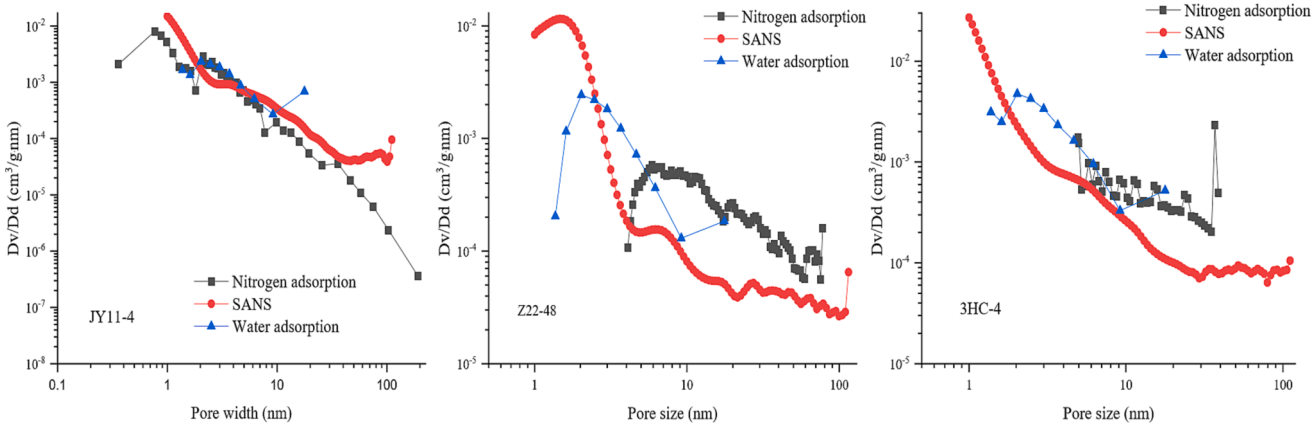

Fig. 6. Pore volume distributions obtained from SANS, WVA, and low-pressure nitrogen adsorption analysis of shale samples.

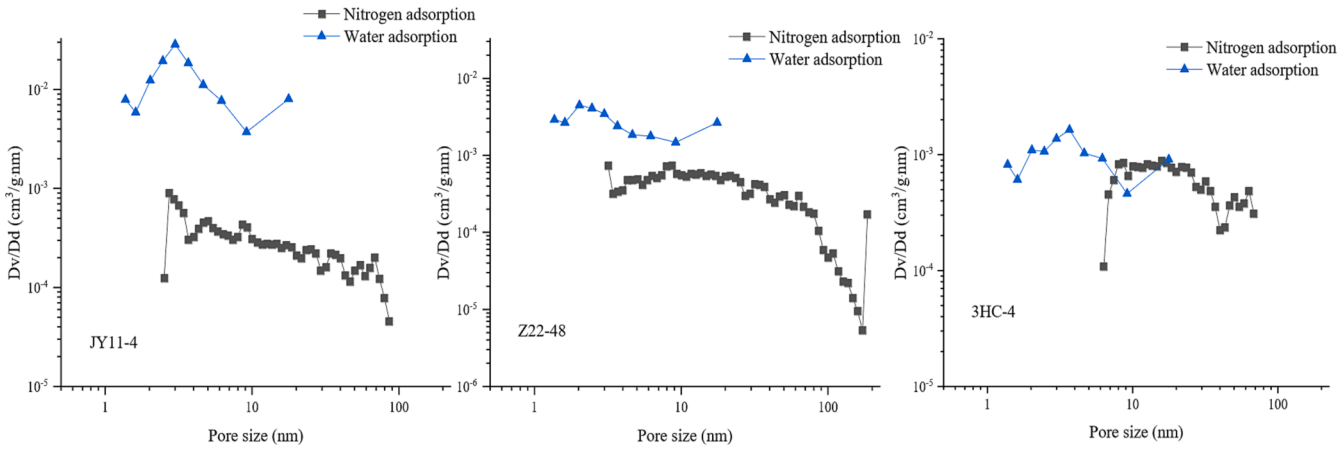

Fig. 7. Pore volume distributions obtained from WVA and low-pressure nitrogen adsorption analysis of organic matter samples.

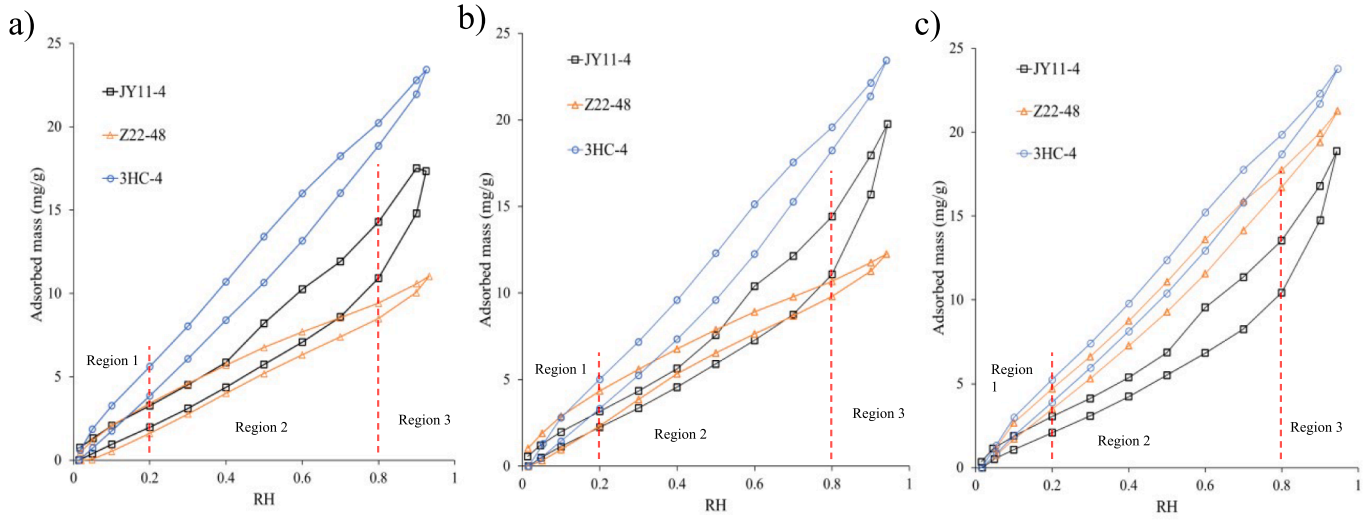

Fig. 8. Water vapor isotherms obtained from shale samples at a) 25 °C b) 35 °C and c) 45 °C.

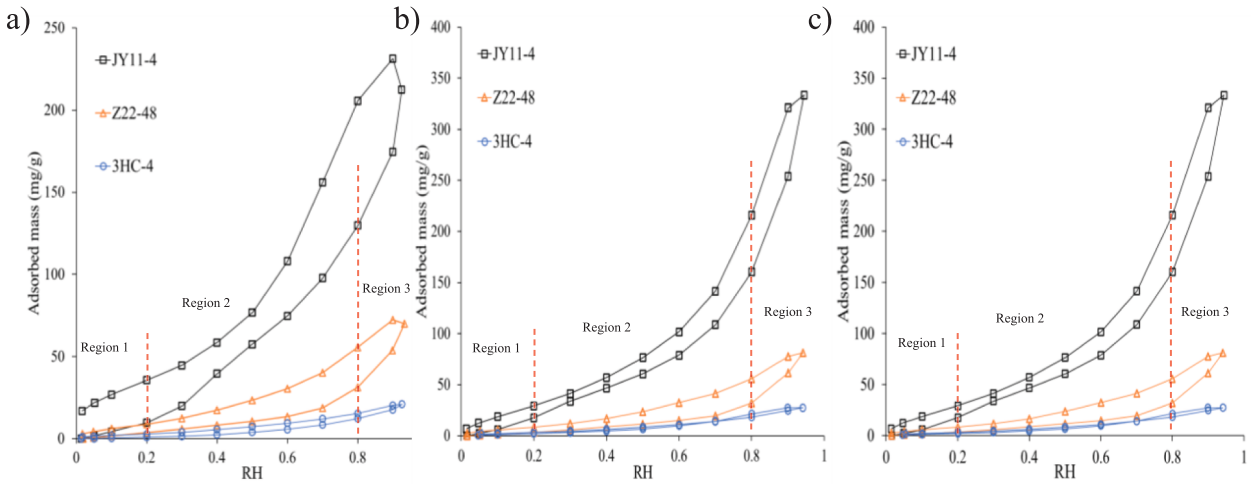

Fig. 9. Water vapor isotherms obtained from organic matter samples at a) 25 °C b) 35 °C and C) 45 °C.

$$\left[\frac{\partial \ln p}{\partial\left(\frac{1}{T}\right)}\right]_V = \frac{1}{R}\Delta H_{ads} \quad (4)$$

Where p represents water vapor pressure (kpa); T temperature (K); R the universal gas constant ($Jmol^{-1}K^{-1}$); and ΔH_{ads} the heat of adsorption within a specified water content V (mg/g).

Table 3
Parameters obtained from fitting WVA isotherms from shale samples.

Model		Parameters	WVA at 25 °C			WVA at 35 °C			WVA at 45 °C		
			JY11-4	Z22-48	3HC-4	JY11-4	Z22-48	3HC-4	JY11-4	Z22-48	3HC-4
GAB		V_m(mg/g)	4.45	17.34	33.49	4.01	26.71	79.16	3.7	24.52	27.4
		C_{GAB}	3.59	1.41	1.46	4.99	2.25	0.6	5.08	1.6	1.6
		K	0.82	0.36	0.38	0.85	0.21	0.32	0.86	0.42	0.42
		R^2	0.9965	0.9956	0.9996	0.9973	0.9959	0.9996	0.9968	0.9998	0.9998
Freundlich	Entire RH	k	14.74	14.93	24.67	14.97	14.1	24.36	13.9	21.37	23.9
		n	0.82	0.61	0.86	0.87	0.84	0.78	0.88	0.88	0.88
		R^2	0.9897	0.9541	0.9992	0.9808	0.99	0.9495	0.9767	0.9985	0.9985
	<70% RH	k	12.63	21.71	24.34	12.21	16.62	23.97	11.01	20.39	22.79
		n	0.87	0.87	0.86	0.95	0.78	0.79	0.98	0.9	0.9
		R^2	0.9992	0.9535	0.9989	0.9994	0.9927	0.987	0.9989	0.9984	0.9984
	>70% RH	k	21.19	12.19	25.85	23.39	13.17	24.45	22.22	22.81	25.5
		n	0.33	0.61	0.70	0.29	0.75	0.66	0.29	0.71	0.71
		R^2	0.9727	0.9844	0.9878	0.9852	0.9873	0.99	0.9777	0.9917	0.9917
Areal hysteresis index (%)			27.60	19.76	11.64	14.79	12.72	7.96	14.18	2.66	3.01

Table 4
Parameters obtained from fitting WVA isotherms obtained from organic matter samples.

Model		Parameters	WVA at 25 °C			WVA at 35 °C			WVA at 45 °C		
			JY11-4	Z22-48	3HC-4	JY11-4	Z22-48	3HC-4	JY11-4	Z22-48	3HC-4
GAB		V_m(mg/g)	71.69	8.1	12.33	51.44	8.22	6.49	42.85	7.53	5.23
		C_{GAB}	1.22	2.32	0.39	2.08	2.35	0.96	2.46	1.9	1.9
		K	0.79	0.96	0.77	0.91	0.97	0.86	0.92	0.89	0.89
		R^2	0.9938	0.9992	0.9985	0.9996	0.9991	0.9997	0.9961	0.9999	0.9999
Freundlich	Entire RH	k	181.73	40.17	14.98	229.82	43.31	17.3	196.74	30.05	19.62
		n	0.61	0.71	0.63	0.63	0.7	0.69	0.68	0.72	0.72
		R^2	0.9857	0.9407	0.9602	0.9783	0.9296	0.9495	0.9669	0.958	0.958
	<70% RH	k	145.71	24.08	9.01	168.56	24.85	10.15	134.71	18.18	12.64
		n	0.66	0.87	0.76	0.71	0.87	0.84	0.78	0.87	0.87
		R^2	0.9856	0.9988	0.9839	0.9979	0.9955	0.987	0.9983	0.9965	0.9965
	>70% RH	k	258.22	96.81	26.66	416.42	113.63	33.82	387.61	53.67	37.3
		n	0.32	0.2	0.29	0.23	0.18	0.26	0.22	0.25	0.25
		R^2	0.9505	0.9908	0.9809	0.9916	0.9991	0.99	0.9892	0.9925	0.9925
Areal hysteresis index (%)			45.28	64.11	39.53	9.96	48.82	26.04	15.37	13.2	13.2

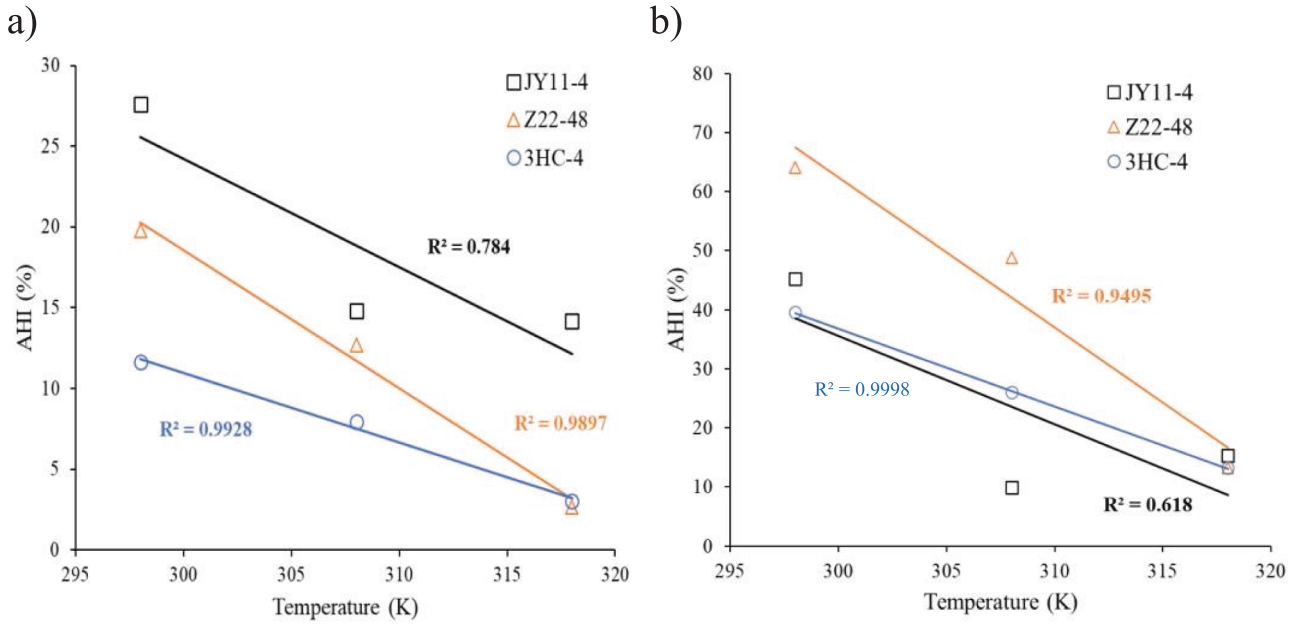

Fig. 10. Plot of Areal Hysteresis Index against temperature for a) shale and b) organic matter samples.

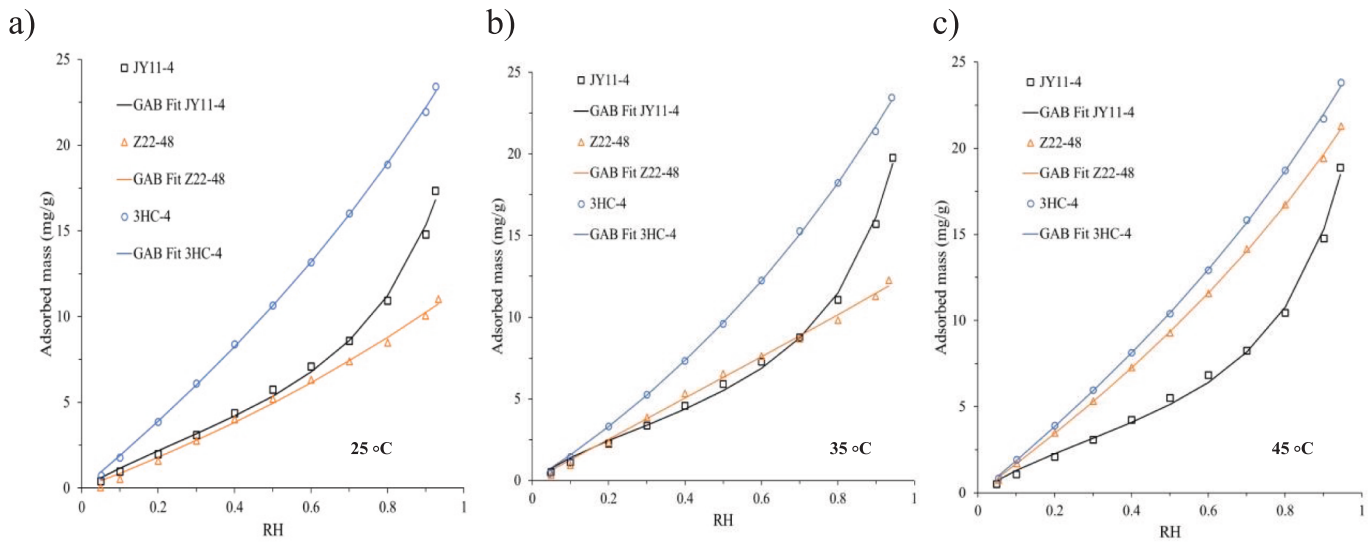

Fig. 11. GAB fitted Water vapor isotherms obtained from shale samples at a) 25 °C b) 35 °C and C) 45 °C.

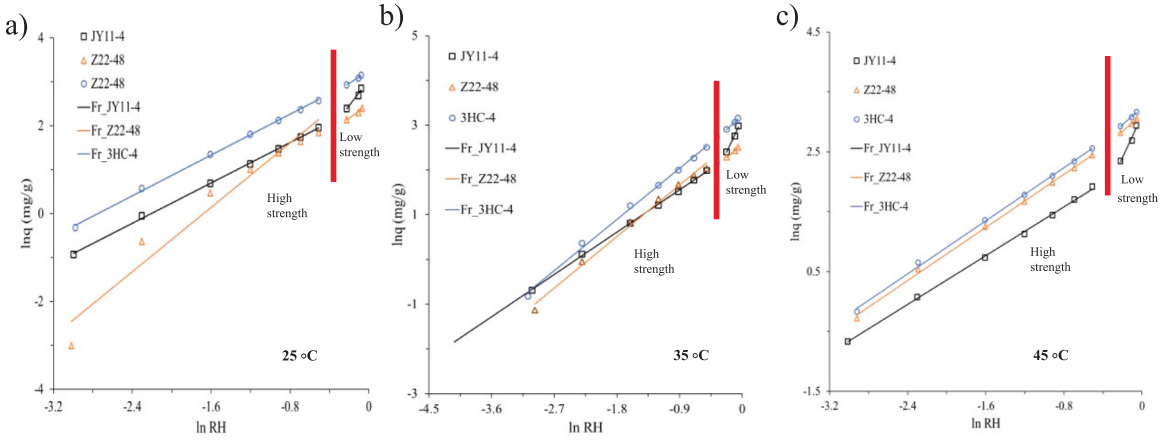

Fig. 12. Freundlich fitted Water vapor isotherms obtained from shale samples at a) 25 °C b) 35 °C and C) 45 °C.

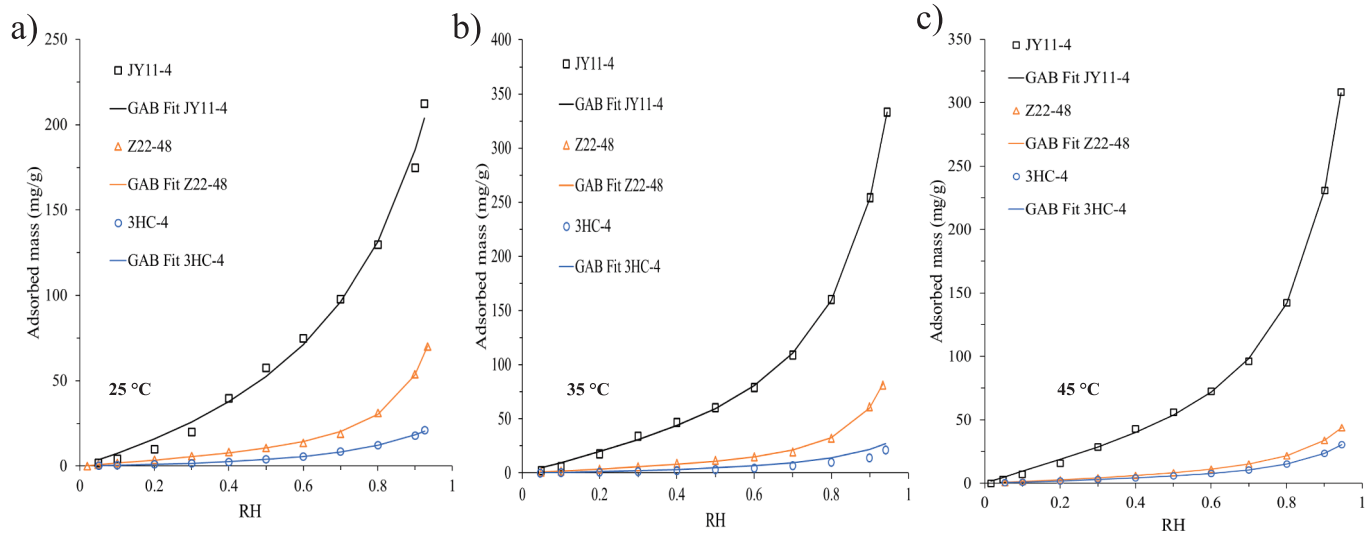

Fig. 13. GAB fitted Water vapor isotherms obtained from organic matter samples at a) 25 °C b) 35 °C and C) 45 °C.

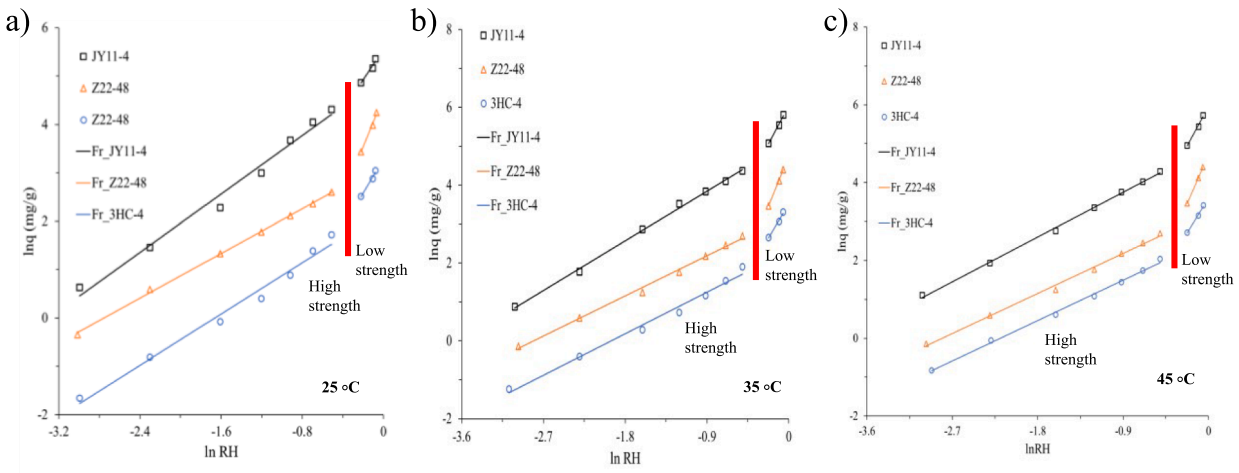

Fig. 14. Freundlich fitted Water vapor isotherms obtained from organic matter samples at a) 25 °C b) 35 °C and C) 45 °C.

Isosteric heat of adsorption (ΔH_{ads}) values obtained from the shale samples over a 0.05 mg/g to 11.03 mg/g water content range are exothermic, and range from 5 kJ/mol to 45 kJ/mol, for the entire samples except those from Z22-48 approaching the pure water latent heat of vaporization (ΔH_{vap}) (42 kJ mol^{-1}) as water content increases (Fig. 15a). While other samples are only characterised by decreasing ΔH_{ads} values at lower water content before approaching ΔH_{vap} as water content increases, a reverse phenomenon is observed generally in lower ΔH_{ads} values in sample Z22-48. In this sample, this value increases with water content while remaining below ΔH_{vap}.

Alike shale samples, ΔH_{ads} values obtained from the organic matter samples over a 0.19 mg/g to 21 mg/g water content range are exothermic, ranging from 16 kJ/mol to 57 kJ/mol (Fig. 15b). While sample Z22-48 is characterised by ΔH_{ads} which increases at lower water content before decreasing to approach ΔH_{vap} after reaching maximum ΔH_{ads} (57 kJ/mol). However, an opposite trend is observed in sample JY11-4 which is characterised by a decreasing ΔH_{ads} at lower water content which then steadily increases while remaining less than ΔH_{vap} after minimum ΔH_{ads} (28 kJ/mol) is attained. Another important phenomenon which contributes to the range of ΔH_{ads} values obtained from the organic matter samples is found in sample 3HC-4 being initially characterised by a reduction in ΔH_{ads} at lower water content which starts to increase and approach ΔH_{vap} when minimum ΔH_{ads} (16 kJ/mol) is reached.

4. Discussion

4.1. Pore structure controls on water adsorption

Studies have used a conjunction of SANS and low pressure nitrogen adsorption experiments to observe shale pore structure controls on water vapor adsorption at higher RH (Sang et al., 2018b), with others using pore volume distributions obtained from WVA and low pressure nitrogen adsorption to make a similar observation (Gao et al., 2022; Hou et al., 2021). Thus, to obtain organic matter and inorganic pore structure controls on water adsorption, we compare shale and organic matter pore structure parameters obtained from SANS, WVA at 25 °C, and N_2 adsorption.

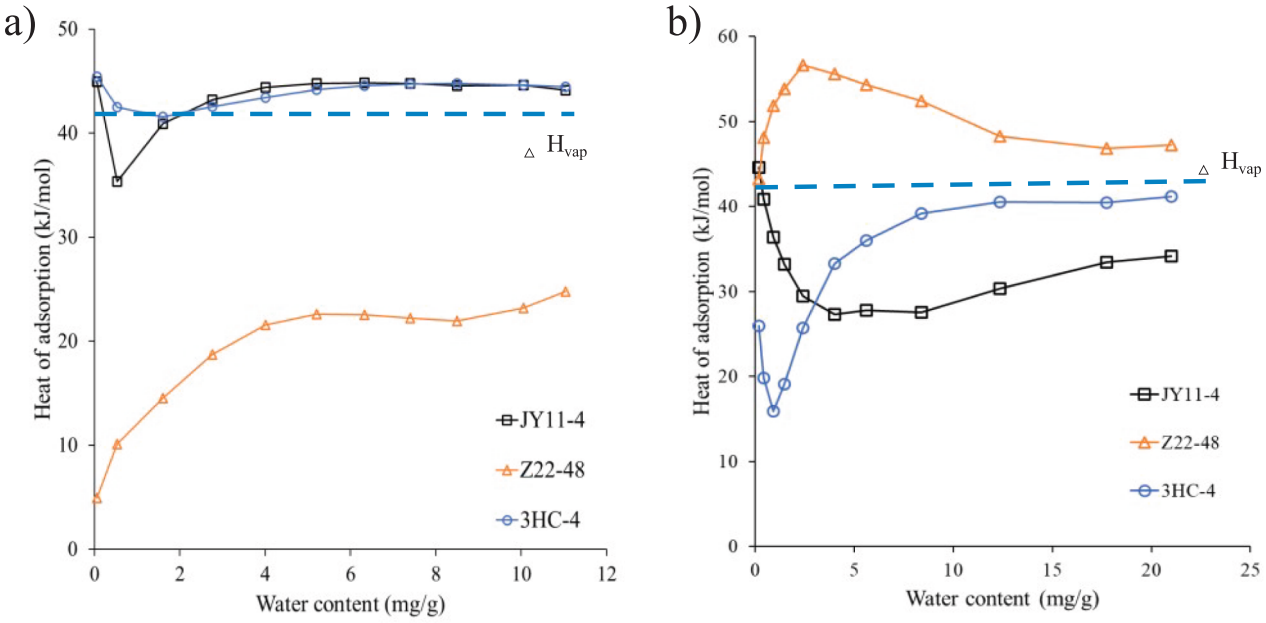

Fig. 15. Isosteric heat of adsorption obtained from a) shale and b) organic matter samples. Pure water latent heat of vaporization (ΔH_{vap}) (42 kJ mol^{-1}) is used to demarcate bound and free water boundary.

Shale WVA isotherms obtained at 25 °C (Fig. 8a) show 3HC-4 > JY11-4 > Z22-48 variation of adsorbed volume at RH > 80% that is similar to mesopore volume and/or porosity variations obtained from low pressure N_2 adsorption (Table 2). SANS is also used to establish a negative relationship between the fraction of closed pores within the shale samples and water adsorption at RH > 80% (Table 2). Studies have shown that both inaccessible and accessible pore measurement can become possible when SANS and low pressure adsorption are combined (Chandra et al., 2020), with others methods following the same measurements technique to observe shales with larger mesopore volumes and nitrogen accessible pores possessing more sites for water condensation at high RH (Sang et al., 2018b). Importantly, since low pressure nitrogen adsorption is unable to characterize pores sizes<1.7 nm (Sang et al., 2019b), a possession of the highest fraction of pores inaccessible to low pressure N_2 adsorption, and an observation of a micropore volume peak (<2nm pore size) in sample Z22-48 obtained from SANS (Fig. 6) both indicate that an inhibition of water condensation at high RH within the sample was due to the presence of a small number of external mesopores, and the presence of bound water in large micropores (less than but close to 2 nm). The latter was also confirmed by this shale sample being characterised by a higher flat scattering background at high Q (Fig. 5). In addition, the higher surface area and closed pore fraction observed in sample Z22-48 is also possibly due to high montmorillonite content which resulted in the formation of inaccessible pores within interlayer spaces that cannot be accessed by the N_2 molecules (Sang et al., 2018a).

Organic matter WVA isotherms at 25 °C (Fig. 9a) reveal a positive relationship between water vapor adsorption and organic matter mesopore volume. Organic matter mesopore controls on water adsorption are also delineated in a negative relationship between adsorbed water volume at all experimental RH and mesopore volume (Table 2), and a reduction in the difference between WVA and N_2 pore volume distributions as organic matter mesopore volume increases (Fig. 7). Organic matter porosity controls are also confirmed by the positive relationship between simulated adsorbed volume and porosity obtained from the kerogen models, and experimental organic matter isotherms revealing a negative relationship between organic matter mesopore volume and water adsorption. The latter is found in organic matter mesopore volume varying in opposite trend compared to a JY11-4 > Z22-48 > 3HC-4 organic matter variation in adsorbed volume, GAB V_m, and Freundlich k. While shale organic matter micropores control water adsorption at lower RH ranges via monolayer coverage, mesopore control is achieved at higher RH values via multilayer adsorption (Zhang et al., 2022).

4.2. Inorganic and organic content controls on water adsorption

Several studies have used WVA isotherms to observe organic and inorganic controls on water adsorption in shale reservoirs (Sang et al., 2019b; Yang et al., 2021a). In this study, WVA isotherms obtained from shales and organic matter along with simulated wet kerogen-quartz nanocomposites reveal an interplay between organic matter and mineral content in regards to water adsorption controls.

4.2.1. Clay controls from WVA and isosteric heat

Inorganic controls are first evidenced by an observation of mixed layer clay content characterised by a positive link to the GAB monolayer moisture content (V_m), and the Fruendlich adsorption capacity constant (k) obtained from the shale samples at high adsorption strength regimes (Table 3). In addition, the Qingshankou shale sample which is characterised by the highest mixed layer clay content, also has the highest adsorbed water volume at all observed maximum RH (Fig. 8, Table 1).

Clay content controls on water adsorption are also obtained from the determination of isosteric heat of adsorption from the shale samples. They reveal all shale samples apart from the Chang 7 formation as characterised by an isosteric heat that declines at low adsorbed water content to a minimum value before gradually approaching the heat of vaporization. Isosteric heat of adsorption can be used to determine the bound water and free water boundary (Quirijns et al., 2005), with studies using isosteric heat of sorption from wheat grains to suggest that an increase in isosteric heat at low moisture content is due to monolayer adsorption induced by highly active polar sites within the sample (Li et al., 2011). Thus, the observed increase in isosteric heat at low water content observed in the Chang 7 shale sample is possibly due to a higher montmorillonite content in the clay interlayers which swells and provides additional primary water adsorption sites (Fig. 15a). This expansion is verified by isotherms from the shale sample with an increase in adsorbed/desorbed volume with increasing experimental temperature (Fig. 8). Furthermore, the occurrence of isosteric heat values obtained from the Chang 7 shale sample beneath the latent heat of vaporization (Fig. 15a) also infers that the observed isotherm changes with temperature are due to monolayer moisture not being tightly bound to the shale surface.

Isosteric heat values obtained from organic matter extracted from the Chang 7 shale are demonstrating an initial increase at lower water content, which then approaches the latent heat of vaporization after attaining a maximum value (Fig. 15b). However, this indication of expansion in primary adsorption sites within organic matter requires further investigations in future studies.

4.2.2. Organic matter oxygen functional group (OFG) water interaction

Studies have reported that organic rich shales can adsorb high water amounts due to the presence of OFGs in organic matter pores (Yang et al., 2021a), which causes a lack of convergence in experimental water vapor isotherms. This phenomenon is attributed to the adsorbed water trapped within the micropore space via hydrogen bonding (Yang et al., 2020b), with others observing a positive relationship between the thermal maturity of organic matter and adsorbed moisture (Li et al., 2020). Furthermore, Bai et al., (2020) recently observed how changes in the OFGs of organic matter at primary adsorption sites can have a positive influence on monolayer water adsorption in shales with very little effect on multi-layered adsorption.

In this study, an indication of organic matter maturity control on water adsorption is signified by highly mature Longmaxi shale sample having higher C_{GAB} and AHI values than less mature samples from other shale reservoirs despite having the lowest clay content. The former observation differs from previous relationship of high C_{GAB} values to water adsorption on primary adsorption sites due to low thermal maturity of organic matter in shales (Yang et al., 2021a). In addition, while the negative relationship observed between AHI and temperature for both shale and organic matter samples (Fig. 10a and 10b) are in agreement with similar observations to temperature controls on AHI variation in shales (Tang et al., 2017), the Longmaxi samples revealed to have less affected by temperature. This is probably due to the higher OFG content of the organic matter in the shale which restricted the desorption of adsorbed water. The higher adsorbed water volume in the Longmaxi organic matter samples is also linked to the presence of more OFG.

Studies have posited on how OFG rich asphaltene in organic matter being pre-adsorbed on the quartz surface could reduce the water affinity of the mineral in shales (Li et al., 2020). Thus, WVA isotherms obtained from the extracted organic matter and kerogen models (Fig. 9 and Fig. 16) reveal that despite being characterised by a high quartz content, water adsorption on the mature Longmaxi shale sample was inhibited by a pre-adsorption of OFG rich organic compounds on the quartz surface.

The control of organic matter OFG on water interaction with quartz is also revealed in nanocomposite water distribution variations with temperature. Snapshots of water distribution in the nanocomposites under increasing temperature reveal water clustering on the quartz surface and adsorbed around kerogen polar groups (Fig. 17). However, due to the larger amounts of OFGs in the Longmaxi kerogen, water adsorbed on the kerogen OFGs become clustered on the quartz surface due to kerogen clustering induced by a temperature increase to 400 K

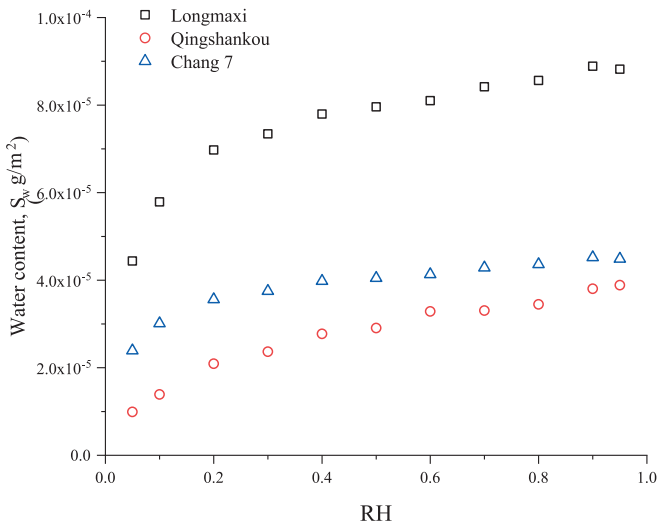

Fig. 16. Water vapor adsorption isotherm obtained from kerogen molecular models.

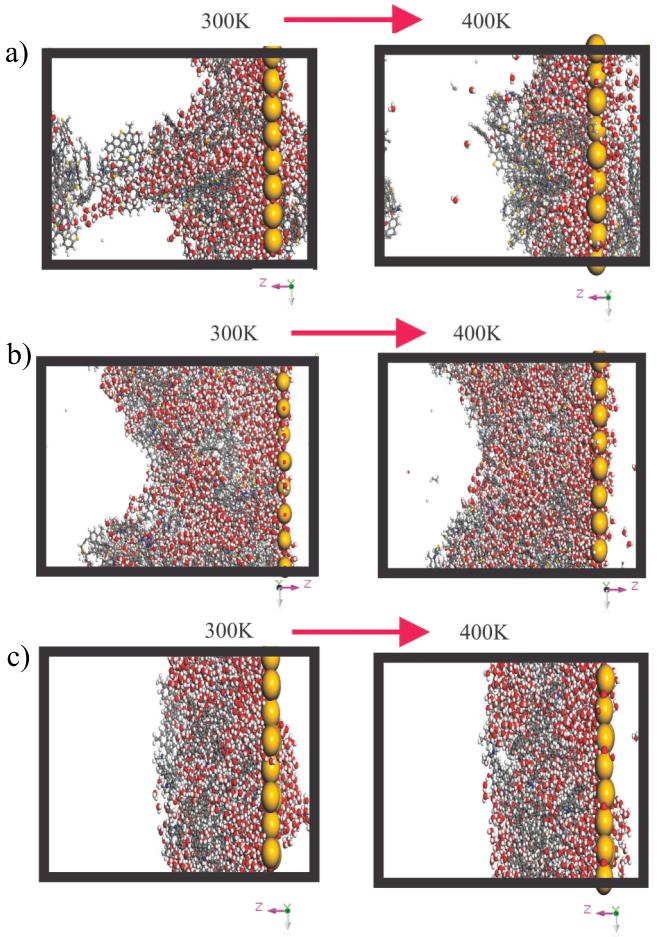

Fig. 17. Temperature influence on water distribution in a) Longmaxi b) Chang 7 and c) Qingshankou nanocomposites.

(Fig. 17a). In addition, compared to profiles obtained from other nanocomposites (Fig. 18b and 18c), two prominent 400 K peaks on concentration profiles obtained from the Longmaxi nanocomposites also reveal a higher clustering of kerogen molecules on the quartz surface as temperature increases (Fig. 18a).

Thus, we speculate that an inhibition of organic matter quartz interaction is facilitated by lower quartz content and organic matter OFG, which in turn caused higher water adsorption observed in the quartz deficient Chang 7 and Qingshankou shale samples. Overall, this explains the quartz content control on water adsorption evidenced by GAB monolayer moisture content V_m varying from quartz deficient shales to quartz rich samples as follows: 3HC-4 > Z22-48 > JY11-4. Thus, while several studies have confirmed that thermal maturity of the organic matter controls water affinity (Hu et al., 2016) and adsorption in shale formations (Yang et al., 2021a), and apart from the fact that carbon aromaticity of the organic material also impacts water wettability in shales (Jagadisan and Heidari, 2020), our observations suggest that its necessary to also consider pre-adsorption of oxygen functional groups of the organic matter on mineral surfaces.

4.3. *Water distribution and CO_2 storage implications*

Shale reservoirs contain water which occur as free water within the pore space or adsorbed pore surface water (Yang et al., 2021b). Studies have observed how the CO_2 storage capacity of shales is controlled by an occurrence of free water in reservoir pores (Hagemann et al., 2016), and adsorbed water on hydrophilic clay nanopores (Jin and Firoozabadi, 2014), with others using WVA isotherms to obtain adsorbed and free water distribution controls in shale reservoirs (Yang et al., 2021b).

In this study, PSD obtained from WVA, SANS, and low-pressure nitrogen adsorption illustrated mesopore control on water adsorption in shales at high RH, with WVA isotherms revealing water distribution as being controlled by the interaction of water with OFGs in organic matter pores, and mixed layer clays. While primary site adsorption is controlled via monolayer coverage induced by the latter, the distribution of water in shale organic matter micropores is attributed to condensation at secondary adsorption sites after primary site adsorption has taken place (Yang et al., 2021b). In addition, water distribution in extracted organic matter analysed in this study was facilitated by decreasing mesopore volume and increase in OFG within organic matter, with quartz controls on water adsorption linked to an interaction with OFGs in organic matter.

The migration of injected CO_2 in shales is inhibited by the occupation or blocking of CO_2 adsorption sites by water adsorbed on hydrophilic clays and organic matter OFGs (Huang et al., 2021). Thus, while CO_2 migration in other samples will be mainly suppressed by water occupation of potential CO_2 adsorption sites in organic matter pores, the presence of pre-adsorbed water induced by the hydrophilic mixed layer montmorillonite will severely stop the migration of injected CO_2 into the Chang 7 shale oil reservoir. This pre-adsorbed water which is not tightly bound to the shale surface, will block potential CO_2 adsorption sites in the shale reservoir during the CO_2 injection process.

5. Conclusion

An experimental and molecular dynamics simulation into water adsorption in marine and lacustrine shales was undertaken to obtain water adsorption controls in shale reservoirs. WVA analysis and low-pressure nitrogen adsorption were performed on shale and organic matter samples along with SANS measurements from shales along with high temperature WVA simulations and water distribution in kerogen-nanocomposites with experimentally verified kerogen models. Based on the results the following key observations on water adsorption controls was seen:

1. While water adsorption in shales at high RH is aided by a decrease in mesopore volume, organic matter is characterised by a similar control at all RH and an increase in oxygen functional groups.
2. Water adsorption at all RH in shales is strongly controlled by the interaction of water with oxygen functional groups in organic matter pores and mixed layered clays, with a negative relationship between

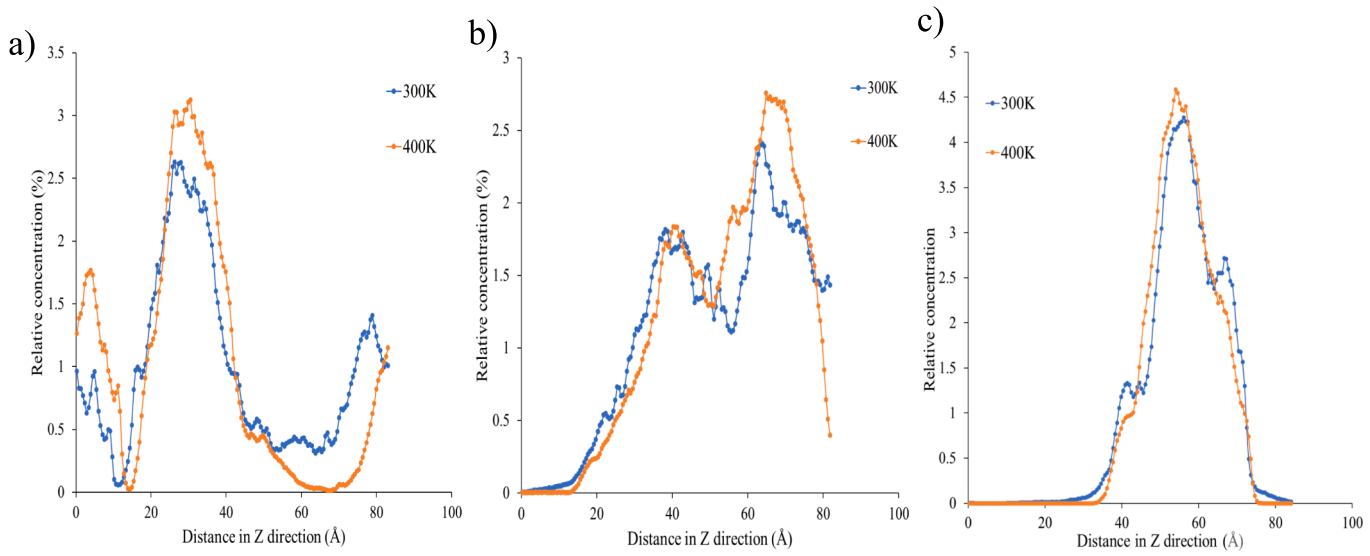

Fig. 18. Concentration profiles obtained from a) Longmaxi b) Chang 7 and c) Qingshankou nanocomposites.

water adsorption and quartz content being due to the interaction of oxygen functional groups within organic matter and quartz.

3. The presence of high amounts of montmorillonite within clay interlayers of shales can induce water distribution not tightly bound to the shale surface.
4. These findings are significant for hydrocarbon exploitation of shale reservoirs and also suggest that CO_2 migration in shale reservoirs will be inhibited by an occurrence of water in potential CO_2 adsorption sites within organic matter pores, and montmorillonite induced water distribution that is not tightly bound to the shale surface.

CRediT authorship contribution statement

Chima Finnian Ukaomah: Writing – original draft. **Mengdi Sun:** Conceptualization, Data curation. **Zhejun Pan:** Resources. **Mehdi Ostadhassan:** Writing – review & editing. **Bo Liu:** Resources. **Qingbang Meng:** Conceptualization. **Mohammed Dahiru Aminu:** Formal analysis. **Michael Fischer:** Methodology.

Declaration of Competing Interest

The authors declare that they have no known competing financial interests or personal relationships that could have appeared to influence the work reported in this paper.

Data availability

The data that has been used is confidential.

Acknowledgements

The authors sincerely thank the National Natural Science Foundation (Grant Nos. 42272159 and 41802146), and the Natural Science Foundation of Heilongjiang Province (TD2021D001) of China, for their financial support. Moreover, we would like to show our gratitude two anonymous reviewers and the editor, for taking the time to read this manuscript and provide us with their comments and feedback that significantly improved the quality of this paper.

References

Anderson, R.B., 1946. Modifications of the Brunauer, Emmett and Teller Equation. J. Am. Chem. Soc. 68, 686–691. https://doi.org/10.1021/ja01208a049.

Arthur, E., Tuller, M., Moldrup, P., De Jonge, L.W., 2016. Evaluation of theoretical and empirical water vapor sorption isotherm models for soils. Water Resour. Res. 52, 190–205. https://doi.org/10.1002/2015WR017681.

Bai, J., Kang, Y., Chen, M., Chen, Z., You, L., Li, X., Chen, G.u., 2020. Impact of surface chemistry and pore structure on water vapor adsorption behavior in gas shale. Chem. Eng. J. 402, 126238.

Berendsen, H.J.C., Postma, J.P.M., van Gunsteren, W.F., DiNola, A., Haak, J.R., 1984. Molecular dynamics with coupling to an external bath. J. Chem. Phys. 81 (8), 3684–3690.

Brunauer, S., Emmett, P.H., Teller, E., 1938. Adsorption of gases in multimolecular layers. J. Am. Chem. Soc. 60, 309–319. https://doi.org/10.1021/ja01269a023.

Cao, H., Lei, Y., Wang, X., Zou, Y.-R., Peng, P., 2021. Molecular structure evolution of Type I kerogen during pyrolysis: Case study from the Songliao Basin. NE China. Mar. Pet. Geol. 134, 105338 https://doi.org/10.1016/j.marpetgeo.2021.105338.

Chandra, D., Vishal, V., Bahadur, J., Sen, D., 2020. A novel approach to identify accessible and inaccessible pores in gas shales using combined low-pressure sorption and SAXS/SANS analysis. Int. J. Coal Geol. 228, 103556.

Chen, M. yi, Yang, Y. pu, Gao, C. hong, Cheng, Y. ping, Wang, J. chun, Wang, N., 2020. Investigation of the fractal characteristics of adsorption-pores and their impact on the methane adsorption capacity of various rank coals via N_2 and H_2O adsorption methods. Energy Sci. Eng. 8, 3228–3243. https://doi.org/10.1002/ese3.727.

Chen, J.i., Xu, Y., Gai, H., Xiao, Q., Wen, J., Zhou, Q., Li, T., 2021. Understanding water accessibility and pore information of overmature marine shales using water vapor sorption. Mar. Pet. Geol. 130, 105120.

Chen, Y., Zhu, Z., Zhang, L., 2019. Control actions of sedimentary environments and sedimentation rates on lacustrine oil shale distribution, an example of the oil shale in the Upper Triassic Yanchang Formation, southeastern Ordos Basin (NW China). Mar. Pet. Geol. 102, 508–520. https://doi.org/10.1016/J.MARPETGEO.2019.01.006.

De Boer, J.H., 1953. Dynamical Character of Adsorption. Oxford University Press.

de la Llave, E., Molinero, V., Scherlis, D.A., 2010. Water filling of hydrophilic nanopores. J. Chem. Phys. 133 (3), 034513.

De La Llave, E., Molinero, V., Scherlis, D.A., 2012. Role of confinement and surface affinity on filling mechanisms and sorption hysteresis of water in nanopores. J. Phys. Chem. C 116, 1833–1840. https://doi.org/10.1021/jp206580z.

Dehghanpour, H., Zubair, H.A., Chhabra, A., Ullah, A., 2012. Liquid intake of organic shales. Energy Fuel 26, 5750–5758. https://doi.org/10.1021/ef3009794.

Dehghanpour, H., Lan, Q., Saeed, Y., Fei, H., Qi, Z., 2013. Spontaneous imbibition of brine and oil in gas shales: Effect of water adsorption and resulting microfractures. Energy Fuel 27, 3039–3049. https://doi.org/10.1021/ef4002814.

Di Lella, A., Desbiens, N., Boutin, A., Demachy, I., Ungerer, P., Bellat, J.-P., Fuchs, A.H., 2006. Molecular simulation studies of water physisorption in zeolites. Phys. Chem. Chem. Phys. 8 (46), 5396.

Dong, D., Shi, Z., Guan, Q., Jiang, S., Zhang, M., Zhang, C., Wang, S., Sun, S., Yu, R., Liu, D., Peng, P., Wang, S., 2018. Progress, challenges and prospects of shale gas exploration in the Wufeng-Longmaxi reservoirs in the Sichuan Basin. Nat. Gas Ind. B 5, 415–424. https://doi.org/10.1016/j.ngib.2018.04.011.

Duan, S., Li, G., 2018. Equilibrium and Kinetics of Water Vapor Adsorption on Shale. J. Energy Resour. Technol. 140, 1–10. https://doi.org/10.1115/1.4040530.

Faisal, H.M.N., Katti, K.S., Katti, D.R., 2021. An insight into quartz mineral interactions with kerogen in Green River oil shale. Int. J. Coal Geol. 238, 103729.

Feng, J., Zhang, B., Feng, Z., Wang, Y., Zhang, J., Fu, X., Sun, Y., Huo, Q., Shao, H., Zeng, H., Qu, B., Chi, H., 2019. Crude oil mobility and its controlling factors in tight sand reservoirs in northern Songliao Basin, East China. Pet. Explor. Dev. 46, 324–334. https://doi.org/10.1016/S1876-3804(19)60012-1.

Finnian Ukaomah, C., Sun, M., Pan, Z., Ostadhassan, M., Liu, B., Xu, Y., Istifanus Madaki, A., Ijeoma Umeobi, H., Dahiru Aminu, M., Yang, B., 2022. An insight into

CO_2 sequestration and EGR in Longmaxi and Niutitang shale formations via experimental analysis. Fuel 324, 124776. https://doi.org/10.1016/J.FUEL.2022.124776.
Freundlich, H., 1931. Of the adsorption of gases. Section II. Kinetics and energetics of gas adsorption. Introductory paper to section II. Trans. Faraday Soc. 28, 195–201.
Gao, Z.-Y., Xiong, S.-L., Wei, L., 2022. The new multistage water adsorption model of Longmaxi Formation shale considering the spatial configuration relationship between organic matter and clay minerals. Pet. Sci. 19 (5), 1950–1963.
Guggenheim, E.A., 1963. Applications of Statistical Mechanics, 1st, Editi. ed. Clarendon Press.
Guo, F., Wang, S., Feng, Q., Yao, X., Xue, Q., Li, X., 2020. Adsorption and absorption of supercritical methane within shale kerogen slit. J. Mol. Liq. 320, 114364 https://doi.org/10.1016/J.MOLLIQ.2020.114364.
Hagemann, B., Panfilov, M., Ganzer, L., 2016. Multicomponent gas rising through water with dissolution in stratified porous reservoirs - Application to underground storage of H_2 and CO_2. J. Nat. Gas Sci. Eng. 31, 198–213. https://doi.org/10.1016/j.jngse.2016.03.019.
Han, H., Cao, Y., Chen, S.-J., Lu, J.-G., Huang, C.-X., Zhu, H.-H., Zhan, P., Gao, Y., 2016. Influence of particle size on gas-adsorption experiments of shales: An example from a Longmaxi Shale sample from the Sichuan Basin, China. Fuel 186, 750–757.
Hazra, B., Wood, D.A., Vishal, V., Singh, A.K., 2018. Pore Characteristics of Distinct Thermally Mature Shales: Influence of Particle Size on Low-Pressure CO_2 and N_2 Adsorption. Energy Fuel 32, 8175–8186. https://doi.org/10.1021/acs.energyfuels.8b01439.
Holmes, R., Rupp, E.C., Vishal, V., Wilcox, J., 2017. Selection of Shale Preparation Protocol and Outgas Procedures for Applications in Low-Pressure Analysis. Energy Fuel 31, 9043–9051. https://doi.org/10.1021/acs.energyfuels.7b01297.
Hoover, W.G., 1985. Canonical dynamics: Equilibrium phase-space distributions. Phys. Rev. A 31 (3), 1695–1697.
Hou, C., Yu, B., Liu, L., Xu, Y., Zhang, Y., Zhang, L., Zhao, J., Zhao, X., Zuo, Q., Sun, M., 2021. Water Uptake Behavior and Influence Factors of Longmaxi Shale: Implications from Water Physisorption and Imbibition Measurements. Energy Fuel 35, 11958–11975. https://doi.org/10.1021/ACS.ENERGYFUELS.1C01413.
Hu, Y., Devegowda, D., Striolo, A., Phan, A., Ho, T.A., Civan, F., Sigal, R., 2015. The dynamics of hydraulic fracture water confined in nano-pores in shale reservoirs. J. Unconv. Oil Gas Resour. 9, 31–39. https://doi.org/10.1016/j.juogr.2014.11.004.
Hu, Y., Devegowda, D., Sigal, R., 2016. A microscopic characterization of wettability in shale kerogen with varying maturity levels. J. Nat. Gas Sci. Eng. 33, 1078–1086. https://doi.org/10.1016/j.jngse.2016.06.014.
Huang, L., Ning, Z., Wang, Q., Qi, R., Li, J., Zeng, Y., Ye, H., Qin, H., 2017. Thermodynamic and Structural Characterization of Bulk Organic Matter in Chinese Silurian Shale: Experimental and Molecular Modeling Studies. Energy Fuel 31, 4851–4865. https://doi.org/10.1021/ACS.ENERGYFUELS.7B00132.
Huang, L., Ning, Z., Wang, Q., Ye, H., Wang, Z., Sun, Z., Qin, H., 2018. Microstructure and adsorption properties of organic matter in Chinese Cambrian gas shale: Experimental characterization, molecular modeling and molecular simulation. Int. J. Coal Geol. 198, 14–28. https://doi.org/10.1016/j.coal.2018.09.001.
Huang, L., Zhou, W., Xu, H., Wang, L., Zou, J., Zhou, Q., 2021. Dynamic fluid states in organic-inorganic nanocomposite: Implications for shale gas recovery and CO_2 sequestration. Chem. Eng. J. 411 https://doi.org/10.1016/j.cej.2021.128423.
Jagadisan, A., Heidari, Z., 2020. Effect of geochemical properties on wettability of kerogen and organic-rich mudrocks. SPE Reserv. Eval. Eng. 23, 758–771. https://doi.org/10.2118/199356-PA.
Jin, Z., Firoozabadi, A., 2014. Effect of water on methane and carbon dioxide sorption in clay minerals by Monte Carlo simulations. Fluid Phase Equilib. 382, 10–20.
Lahn, L., Bertier, P., Seemann, T., Stanjek, H., 2020. Distribution of sorbed water in the pore network of mudstones assessed from physisorption measurements. Microporous Mesoporous Mater. 295, 109902 https://doi.org/10.1016/j.micromeso.2019.109902.
Li, X., Cao, Z., Wei, Z., Feng, Q., Wang, J., 2011. Equilibrium moisture content and sorption isosteric heats of five wheat varieties in China. J. Stored Prod. Res. 47, 39–47. https://doi.org/10.1016/J.JSPR.2010.10.001.
Li, J., Li, X., Wu, K., Feng, D., Zhang, T., Zhang, Y., 2017. Thickness and stability of water film confined inside nanoslits and nanocapillaries of shale and clay. Int. J. Coal Geol. 179, 253–268. https://doi.org/10.1016/j.coal.2017.06.008.
Li, S., Shi, Z., Liu, X., Yang, S., Deng, X., Liu, G., Li, J., 2013. Quantitative analysis of the Mesozoic abnormal low pressure in Ordos Basin. Pet. Explor. Dev. 40, 566–571. https://doi.org/10.1016/S1876-3804(13)60074-9.
Li, P., Zhang, J., Rezaee, R., Dang, W., Tang, X., Nie, H., Chen, S., 2021. Effect of adsorbed moisture on the pore size distribution of marine-continental transitional shales: Insights from lithofacies differences and clay swelling. Appl. Clay Sci. 201, 105926.
Liang, L., Luo, D., Liu, X., Xiong, J., 2016. Experimental study on the wettability and adsorption characteristics of Longmaxi Formation shale in the Sichuan Basin. China. J. Nat. Gas Sci. Eng. 33, 1107–1118. https://doi.org/10.1016/j.jngse.2016.05.024.
Loucks, R.G., Reed, R.M., Ruppel, S.C., Jarvie, D.M., 2009. Morphology, genesis, and distribution of nanometer-scale pores in siliceous mudstones of the mississippian barnett shale. J. Sediment. Res. 79, 848–861. https://doi.org/10.2110/jsr.2009.092.
Lowell, S., Shields, J.E., Thomas, M.A., Thommes, M., 2004. Characterization of Porous Solids and Powders: Surface Area, Pore Size and Density. Springer Science+Business Media, New York. https://doi.org/10.1007/978-1-4020-2303-3.
Mastalerz, M., He, L., Melnichenko, Y.B., Rupp, J.A., 2012. Porosity of coal and shale: Insights from gas adsorption and SANS/USANS techniques. Energy Fuel 26 (8), 5109–5120.
Mastalerz, M., Hampton, L.B., Drobniak, A., Loope, H., 2017. Significance of analytical particle size in low-pressure N_2 and CO_2 adsorption of coal and shale. Int. J. Coal Geol. 178, 122–131. https://doi.org/10.1016/j.coal.2017.05.003.
National Institute of Standards and Technology, 2018. SAT-TMMC: Liquid-Vapor coexistence properties - SPC/E Water (LRC) [WWW Document]. URL https://www.nist.gov/mml/csd/informatics/sat-tmmc-liquid-vapor-coexistence-properties-spce-water-lrc.
Okiongbo, K.S., Aplin, A.C., Larter, S.R., 2005. Changes in Type II Kerogen Density as a Function of Maturity: Evidence from the Kimmeridge Clay Formation. https://doi.org/10.1021/EF050194.
Quirijns, E.J., Van Boxtel, A.J.B., Van Loon, W.K.P., Van Straten, G., 2005. Sorption isotherms, GAB parameters and isosteric heat of sorption. J. Sci. Food Agric. 85, 1805–1814. https://doi.org/10.1002/JSFA.2140.
Radliński, A.P., Boreham, C.J., Lindner, P., Randl, O., Wignall, G.D., Hinde, A., Hope, J.M., 2000. Small angle neutron scattering signature of oil generation in artificially and naturally matured hydrocarbon source rocks. Org. Geochem. 31, 1–14. https://doi.org/10.1016/S0146-6380(99)00128-X.
Radlinski, A.P., Radlinska, E.Z., Agamalian, M., Wignall, G.D., Lindner, P., Randl, O.G., 1999. Fractal geometry of rocks. Phys. Rev. Lett. 82, 3078–3081. https://doi.org/10.1103/PhysRevLett.82.3078.
Sang, G., Liu, S., Zhang, R., Elsworth, D., He, L., 2018. Nanopore characterization of mine roof shales by SANS, nitrogen adsorption, and mercury intrusion: Impact on water adsorption/retention behavior. Int. J. Coal Geol. 200, 173–185. https://doi.org/10.1016/j.coal.2018.11.009.
Sang, G., Liu, S., Elsworth, D., 2019a. Water vapor sorption properties of Illinois shales under dynamic water vapor conditions: experimentation and modeling. Water Resour. Res. 55 (8), 7212–7228.
Sang, G., Liu, S., Elsworth, D., 2019b. Water Vapor Sorption Properties of Illinois Shales Under Dynamic Water Vapor Conditions: Experimentation and Modeling. Water Resour. Res. 55, 7212–7228. https://doi.org/10.1029/2019WR024992.
Sang, G., Liu, S., Elsworth, D., Yang, Y., Fan, L., 2020a. Evaluation and modeling of water vapor sorption and transport in nanoporous shale. Int. J. Coal Geol. 228, 103553 https://doi.org/10.1016/j.coal.2020.103553.
Sang, G., Liu, S., Elsworth, D., Zhang, R., Bleuel, M., 2020b. Pore-Scale Water Vapor Condensation Behaviors in Shales: An Experimental Study. Transp Porous Med 135 (3), 713–734.
Seemann, T., Bertier, P., Krooss, B.M., Stanjek, H., 2017. Water vapour sorption on mudrocks. Geol. Soc. Spec. Publ. 454, 201–233. https://doi.org/10.1144/SP454.8.
Shen, W., Li, X., Lu, X., Guo, W., Zhou, S., Wan, Y., 2018. Experimental study and isotherm models of water vapor adsorption in shale rocks. J. Nat. Gas Sci. Eng. 52, 484–491. https://doi.org/10.1016/j.jngse.2018.02.002.
Sing, K.S.W., Everett, D.H., Haul, R.A.W., Moscou, L., Pierotti, R.A., Rouquerol, J., Siemieniewska, T., 1985. Reporting Physisorption Data for Gas/Solid Systems with Special Reference to the Determination of Surface Area and Porosity. Pure Appl. Chem. 57, 603–619. https://doi.org/10.1351/pac198557040603.
Singh, D.P., Chandra, D., Vishal, V., Hazra, B., Sarkar, P., 2021. Impact of Degassing Time and Temperature on the Estimation of Pore Attributes in Shale. Energy Fuel 35, 15628–15641. https://doi.org/10.1021/acs.energyfuels.1c02201.
Striolo, A., Gubbins, K.E., Gruszkiewicz, M.S., Cole, D.R., Simonson, J.M., Chialvo, A.A., Cummings, P.T., Burchell, T.D., More, K.L., 2005. Effect of Temperature on the Adsorption of Water in Porous Carbons. Langmuir 21, 9457–9467. https://doi.org/10.1021/la051120t.
Sun, H., 1998. Compass: An ab initio force-field optimized for condensed-phase applications - Overview with details on alkane and benzene compounds. J. Phys. Chem. B 102, 7338–7364. https://doi.org/10.1021/JP980939V.
Sun, M., Yu, B., Hu, Q., Chen, S., Xia, W., Ye, R., 2016. Nanoscale pore characteristics of the Lower Cambrian Niutitang Formation Shale: A case study from Well Yuke #1 in the Southeast of Chongqing. China. Int. J. Coal Geol. 154–155, 16–29. https://doi.org/10.1016/j.coal.2015.11.015.
Sun, M., Yu, B., Hu, Q., Zhang, Y., Li, B., Yang, R., Melnichenko, Y.B., Cheng, G., 2017. Pore characteristics of Longmaxi shale gas reservoir in the Northwest of Guizhou, China: Investigations using small-angle neutron scattering (SANS), helium pycnometry, and gas sorption isotherm. Int. J. Coal Geol. 171, 61–68. https://doi.org/10.1016/j.coal.2016.12.004.
Sun, M., Wen, J., Pan, Z., Liu, B., Blach, T.P., Ji, Y., Hu, Q., Yu, B., Wu, C., Ke, Y., 2022. Pore accessibility by wettable fluids in overmature marine shales of China: Investigations from contrast-matching small-angle neutron scattering (CM-SANS). Int. J. Coal Geol. 255, 103987 https://doi.org/10.1016/J.COAL.2022.103987.
Tang, X., Ripepi, N., Valentine, K.A., Keles, C., Long, T., Gonciaruk, A., 2017. Water vapor sorption on Marcellus shale: measurement, modeling and thermodynamic analysis. Fuel 209, 606–614. https://doi.org/10.1016/j.fuel.2017.07.062.
Thommes, M., Kaneko, K., Neimark, A.V., Olivier, J.P., Rodriguez-Reinoso, F., Rouquerol, J., Sing, K.S.W., 2015. Physisorption of gases, with special reference to the evaluation of surface area and pore size distribution (IUPAC Technical Report). Pure Appl. Chem. 87, 1051–1069. https://doi.org/10.1515/pac-2014-1117.
Tokunaga, T.K., 2009. Hydraulic properties of adsorbed water films in unsaturated porous media. Water Resour. Res. 45, 1–9. https://doi.org/10.1029/2009WR007734.
Ungerer, P., Collell, J., Yiannourakou, M., 2015. Molecular modeling of the volumetric and thermodynamic properties of kerogen: Influence of organic type and maturity. Energy Fuel 29, 91–105. https://doi.org/10.1021/EF502154K.
Wan, K., He, Q., Miao, Z., Liu, X., Huang, S., 2016. Water desorption isotherms and net isosteric heat of desorption on lignite. Fuel 171, 101–107. https://doi.org/10.1016/j.fuel.2015.12.054.

Wang, T., Tian, S., Li, G., Sheng, M., Ren, W., Liu, Q., Tan, Y., Zhang, P., 2019. Experimental study of water vapor adsorption behaviors on shale. Fuel 248, 168–177. https://doi.org/10.1016/j.fuel.2019.03.029.

Wu, Z., Xu, Z., 2022. Experimental and molecular dynamics investigation on the pyrolysis mechanism of Chang 7 type-II oil shale kerogen. J. Pet. Sci. Eng. 209, 109878 https://doi.org/10.1016/J.PETROL.2021.109878.

Xu, J., Liu, Z., Bechtel, A., Sachsenhofer, R.F., Jia, J., Meng, Q., Sun, P., 2019. Organic matter accumulation in the Upper Cretaceous Qingshankou and Nenjiang Formations, Songliao Basin (NE China): Implications from high-resolution geochemical analysis. Mar. Pet. Geol. 102, 187–201. https://doi.org/10.1016/j.marpetgeo.2018.12.037.

Yang, R., Jia, A., He, S., Hu, Q., Dong, T., Hou, Y., Yan, J., 2020a. Water adsorption characteristics of organic-rich Wufeng and Longmaxi Shales, Sichuan Basin (China). J. Pet. Sci. Eng. 193, 107387.

Yang, R., Jia, A., He, S., Hu, Q., Dong, T., Hou, Y., Yan, J., 2020b. Water adsorption characteristics of organic-rich Wufeng and Longmaxi Shales, Sichuan Basin (China). J. Pet. Sci. Eng. 193, 107387 https://doi.org/10.1016/j.petrol.2020.107387.

Yang, R., Jia, A., Hu, Q., Guo, X., Sun, M., 2020c. Particle size effect on water vapor sorption measurement of organic shale: One example from dongyuemiao member of lower jurassic ziliujing formation in jiannan area of china. Adv. Geo-Energy Res. 4, 207–218. https://doi.org/10.26804/ager.2020.02.09.

Yang, R., Jia, A., He, S., Hu, Q., Sun, M., Dong, T., Hou, Y., Zhou, S., 2021a. Experimental investigation of water vapor adsorption isotherm on gas-producing Longmaxi shale: Mathematical modeling and implication for water distribution in shale reservoirs. Chem. Eng. J. 406, 125982.

Yang, R., Jia, A., He, S., Hu, Q., Sun, M., Dong, T., Hou, Y., Zhou, S., 2021b. Experimental investigation of water vapor adsorption isotherm on gas-producing Longmaxi shale: Mathematical modeling and implication for water distribution in shale reservoirs. Chem. Eng. J. 406, 125982 https://doi.org/10.1016/j.cej.2020.125982.

Zhang, C., Wang, J., Chen, R., 2021. Water adsorption isotherms on soil external particle surface by molecular simulation. Comput. Geotech. 139, 104432 https://doi.org/10.1016/j.compgeo.2021.104432.

Zhang, J., Xu, X., Bai, J., Liu, W., Chen, S., Liu, C., Li, Y., 2020a. Enrichment and exploration of deep lacustrine shale oil in the first member of Cretaceous Qingshankou Formation, southern Songliao Basin, NE China. Pet. Explor. Dev. 47, 683–698. https://doi.org/10.1016/S1876-3804(20)60085-4.

Zhang, C., Yao, Y., Swennen, R., Wu, H., 2022. Combined effects of the chemical structure and nanopore development on water vapor/liquid adsorption in shale kerogen. Colloids Surfaces A Physicochem. Eng. Asp. 653, 129920.

Zhang, Y., Yu, B., Pan, Z., Hou, C., Zuo, Q., Sun, M., 2020b. Effect of thermal maturity on shale pore structure: A combined study using extracted organic matter and bulk shale from Sichuan Basin. China. J. Nat. Gas Sci. Eng. 74, 103089 https://doi.org/10.1016/J.JNGSE.2019.103089.

Zhao, W.B., Hu, S.Y., Deng, X.Q., Bai, B., Tao, S.Z., Sun, B., Wang, Q.R., Cheng, D.X., 2021. Physical property and hydrocarbon enrichment characteristics of tight oil reservoir in Chang 7 division of Yanchang Formation, Xin'anbian oilfield, Ordos Basin. China. Pet. Sci. 18, 1294–1304. https://doi.org/10.1016/J.PETSCI.2020.07.001.

Zhou, Y., Sun, W., Chu, W., Liu, X., Jing, F., Xue, Y., 2016. Theoretical insight into the enhanced CH_4 desorption via H_2O adsorption on different rank coal surfaces. J. Energy Chem. 25, 677–682. https://doi.org/10.1016/j.jechem.2016.04.011.

Zolfaghari, A., Dehghanpour, H., 2015. A comparative study of pore size distribution in gas shales. Soc. Pet. Eng. - SPE Asia Pacific Unconv. Resour. Conf. Exhib. i, 9–11.

Zolfaghari, A., Dehghanpour, H., Holyk, J., 2017a. Water sorption behaviour of gas shales: I. Role of clays. Int. J. Coal Geol. 179, 130–138. https://doi.org/10.1016/j.coal.2017.05.008.

Zolfaghari, A., Dehghanpour, H., Xu, M., 2017b. Water sorption behaviour of gas shales: II. Pore size distribution. Int. J. Coal Geol. 179, 187–195. https://doi.org/10.1016/j.coal.2017.05.009.